Engineering Science and Technology, an International Journal 83 (2026) 102542

Contents lists available at ScienceDirect

Engineering Science and Technology, an International Journal

journal homepage: www.elsevier.com/locate/jestch

Full Length Article

Performance-oriented seismic retrofit of a Cliff-mounted steel–glass observation platform under near-source ground motions: viscous damping strategies and targeted section enhancement

Adnan Kiral [a], Zeliha Tonyali [a,*], Maziar Fahimi Farzam [b,c]

[a] Recep Tayyip Erdogan University, Faculty of Engineering and Architecture, Department of Civil Engineering, Rize 53100, Türkiye
[b] University of Maragheh, Faculty of Engineering, Department of Civil Engineering, Maragheh 55181-83111, Iran
[c] Sahand University of Technology, Faculty of Civil Engineering, Tabriz, Iran

ARTICLE INFO

Keywords:
Cliff-mounted glass observation platform
Fluid viscous damper
Near-source ground motion
Performance-oriented seismic retrofit
Demand-to-capacity ratio
Hybrid strengthening

ABSTRACT

Cliff-mounted steel–glass observation platforms may be earthquake-sensitive because of their slender supports, low inherent damping, and elevated mass. This study presents a numerical proof of concept for retrofitting the Oylat Glass Observation Platform in Türkiye with fluid viscous dampers (FVDs). To the authors' knowledge, and within the literature reviewed, this is the first reported FVD retrofit study for a freestanding or cliff-mounted steel–glass observation platform. Three spectrally matched near-source records from the 2023 Kahramanmaraş earthquake sequence were applied simultaneously in two horizontal directions. Direct-integration response-history analyses were performed. Four strategies were compared. Strategy 1 used all feasible external and internal FVDs. Strategy 2 controlled the columns first and then added deck dampers one at a time. Strategy 3 used only external FVDs to control the columns. Strategy 4 combined external FVDs with ring-beam strengthening. In each strategy, Design Methodology II (DM-II) iteratively adjusted the active damper coefficients using the governing demand-to-capacity (D/C) ratio. Strategies 1, 2, and 4 kept all audited members at D/C $\leq$ 0.80. Their maximum D/C ratios were 0.7991, 0.7820, and 0.7882, respectively. Strategy 3 met its column-control objective but did not control the full deck. Its maximum D/C ratio was 2.8292. Strategy 2 gave the lowest maximum D/C. Strategy 4 gave the most uniform outer-deck displacement. These results establish a proof-of-concept benchmark for future FVD placement and sizing algorithms.

1. Introduction

The global development of slender and long-span structures is exemplified by the Grand Canyon Skywalk (USA), the 516 m Arouca Bridge (Portugal) [1], and the glass-bottom Zhangjiajie Glass Bridge (China) [2,3]. Together with facilities such as the First Cliff Walk (Switzerland), these projects demonstrate how structural efficiency can be combined with architectural transparency and panoramic visitor experience. Similar growth is evident in Türkiye, where Glass Observation Platforms (GOPs) have increasingly become regional landmarks since 2012. Representative GOPs in Türkiye and other countries are shown in Fig. 1. Although these configurations provide distinctive aesthetic and functional benefits, their slender load paths and flexible geometries can make them sensitive to dynamic and seismic excitation.

A recent inventory lists 26 active glass observation decks in Türkiye as of 2025 [4]. They range from the Safranbolu Crystal Terrace to the Kirazlıdere Glass Observation Deck in Isparta. Kirazlıdere had received more than one million visitors by June 2025 [4]. These systems have several structural forms. Some are cantilevered decks attached to buildings [5–7]. Others are cliff- or canyon-mounted platforms, long-span pedestrian bridges, or glass-bottom walkways [3,10,11]. Some are lightweight elevated platforms supported by trusses or cables [12]. Laminated glass can add material- and interface-sensitive vibration effects [8]. Despite their different forms, these structures often have slender load paths, high flexibility, and low inherent damping. Their response to vibration, wind, and earthquakes is therefore important [10,12,13].

A wide range of passive, active, semi-active, and hybrid systems has been developed to reduce structural vibration [11,14,15]. Active and semi-active systems can adapt to changing motion. However, they need

* Corresponding author.
E-mail address: zeliha.tonyali@erdogan.edu.tr (Z. Tonyali).

https://doi.org/10.1016/j.jestch.2026.102542
Received 1 May 2026; Received in revised form 18 August 2026; Accepted 15 September 2026
2215-0986/© 2026 The Author(s). Published by Elsevier B.V. on behalf of Karabuk University. This is an open access article under the CC BY license (http://creativecommons.org/licenses/by/4.0/).



a) Safranbolu Crystal Terrace (Karabük Province, Türkiye)
b) Ulubey Glass Terrace (Uşak Province, Türkiye)
c) Azdavay Çatak Terrace (Kastamonu Province, Türkiye)
d) Kirazlıdere glass observation platform (Isparta Province, Türkiye)
e) Xiangyun observation platform (Henan Province, China)
f) Shilinxia cantilever viewing platform (Beijing Province, China)
g) Grand Canyon skywalk (Arizona, USA)
h) Sky Mirror glass observation platform (Hubei Province, China)

Fig. 1. Representative cantilevered glass observation platforms in Türkiye and other countries.

power, sensors, control hardware, and maintenance. These needs can limit their use in remote or slender tourist structures. Their nonlinear models and sensor–actuator coordination can also be complex [16]. Passive systems include tuned mass dampers [17], viscoelastic dampers [18], and nonlinear energy sinks [19]. They remain attractive because they are reliable. Hybrid systems combine supplemental damping with another seismic intervention [9]. Viscous devices include linear and nonlinear fluid viscous dampers [20,21], viscous wall dampers [22,23], viscous inerter dampers [24], and tuned viscous mass dampers [25,26] (Fig. 2). These devices dissipate energy through velocity-dependent forces. Several studies report large reductions in displacement and acceleration [21,27].

Fluid viscous dampers developed from hydraulic recoil and shock-isolation devices. They were later used in civil structures [21,28,29]. Commercial structural use expanded during the 1990s. These devices add energy dissipation without a similar increase in the elastic stiffness of the main frame. Their force depends mainly on velocity and is approximately out of phase with displacement. This behaviour is useful for slender observation platforms. Adding substantial mass or global stiffness to such platforms may reduce architectural transparency or attract greater seismic forces.

The effectiveness of FVDs depends strongly on their size and location [20]. The literature provides established FVD design and optimisation methods for conventional buildings and bridges [20,30–32]. In contrast, the cited studies on observation decks and transparent pedestrian structures mainly discuss inventories, architecture, human-induced vibration, or serviceability [2–5,33]. In the literature reviewed here, dedicated evidence on the seismic retrofit of freestanding or cliff-mounted steel–glass observation platforms with FVDsis limited. A tower-supported circular platform is not a conventional multi-storey frame. A damper can change the support load path, redistribute demand in the ring–radial deck, and shift the governing member. The tower and deck must therefore be checked again after each intervention.

The 2023 Kahramanmaraş earthquake sequence caused severe

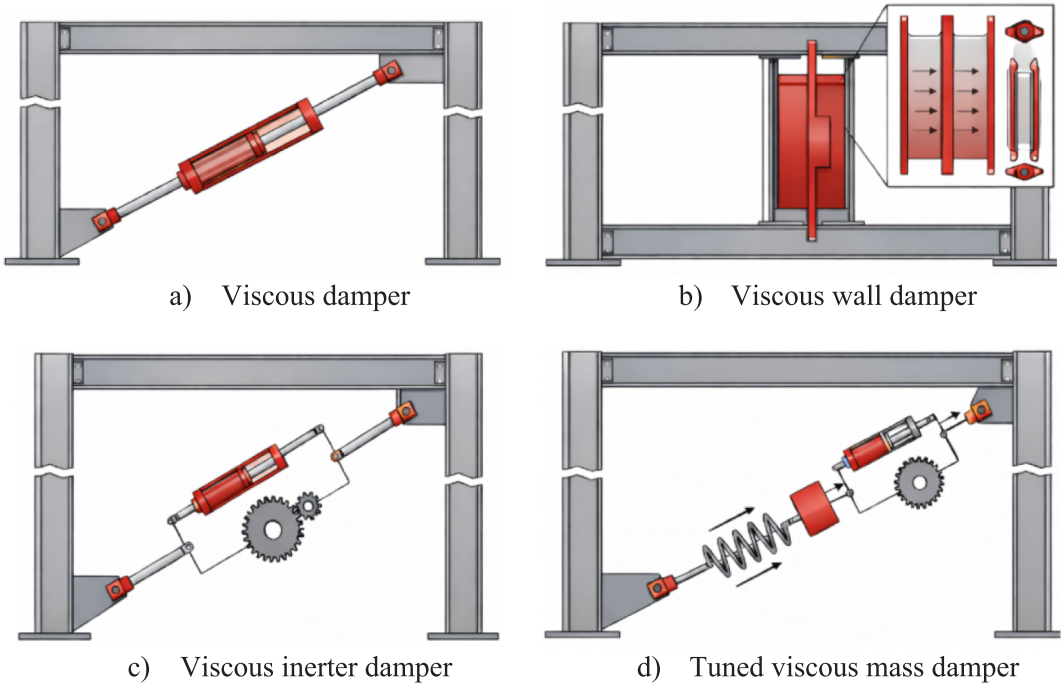

Fig. 2. Schematic examples of viscous damping devices: (a) fluid viscous damper, (b) viscous wall damper, (c) viscous inerter damper, and (d) tuned viscous mass damper.

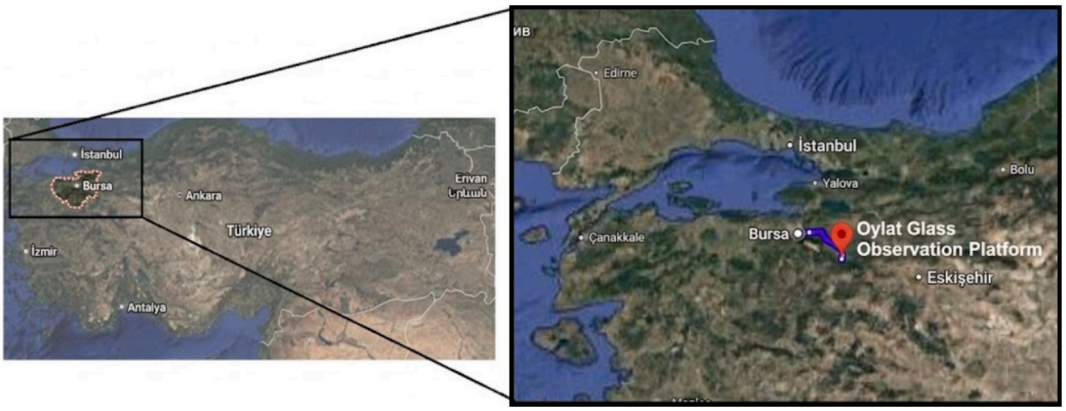

Fig. 3. Location of the Oylat Glass Observation Platform in Bursa Province on the Earthquake Hazard Map of Türkiye (modified after AFAD maps [49]).

structural and geotechnical effects in Türkiye. Near-source demands were also pronounced. Post-earthquake reports from Türkiye and another recent strong earthquake show that local deficiencies and irregular load paths can concentrate structural damage [34–38,40–42]. Previous experimental and analytical studies also show that pulse-like near-source motions can strongly affect long-period structures and structures with viscous dampers [39,43–48]. The response depends on the structural period, input direction, and damper nonlinearity. To address this gap, this study develops a seismic-retrofit framework for a cliff-mounted steel–GOP under selected near-source motions. The framework treats the tower–support system and the torsion-sensitive circular deck as two connected control domains. The vertical support columns represent the tower domain during damper sizing. The four strategies differ in three ways. They use dampers at different locations and stages. They also differ in whether existing dampers are retuned after force redistribution. Finally, remaining deck demand is treated by either more damping or section strengthening.

To the authors' knowledge, and within the literature reviewed, this is the first reported numerical proof of concept for the seismic retrofit of a freestanding or cliff-mounted steel–GOP with FVDs. The contribution is the decision sequence developed for this structural system. The sequence treats the support columns and circular deck as connected control regions. Str#1 activates the full feasible damper layout. Str#2 controls the columns first and then adds deck dampers one at a time. Str#3 stops after column control. Str#4 combines external column dampers with ring-beam strengthening. The structure is rechecked after each change because the force path can shift. The four strategies were implemented as transparent engineering iterations because the reviewed literature provided no established FVD procedure for this platform type. DM-II updates the damper coefficients within each strategy stage. The strategy logic determines when a damper is added, retained, or retuned and when section strengthening is introduced. Each record is processed independently. The final configuration includes all locations and strengthening regions required by the records. It uses the largest required value at each location or region. The final configuration is then reanalysed under every record. These procedures are not claimed to be universal optimisation algorithms. Instead, they provide a reproducible proof-of-concept benchmark. Future studies can use this benchmark to



(a) (b)

Fig. 4. The Oylat Glass Observation Platform: (a) top view showing the circular deck geometry and (b) side view showing the lattice-tower support system.

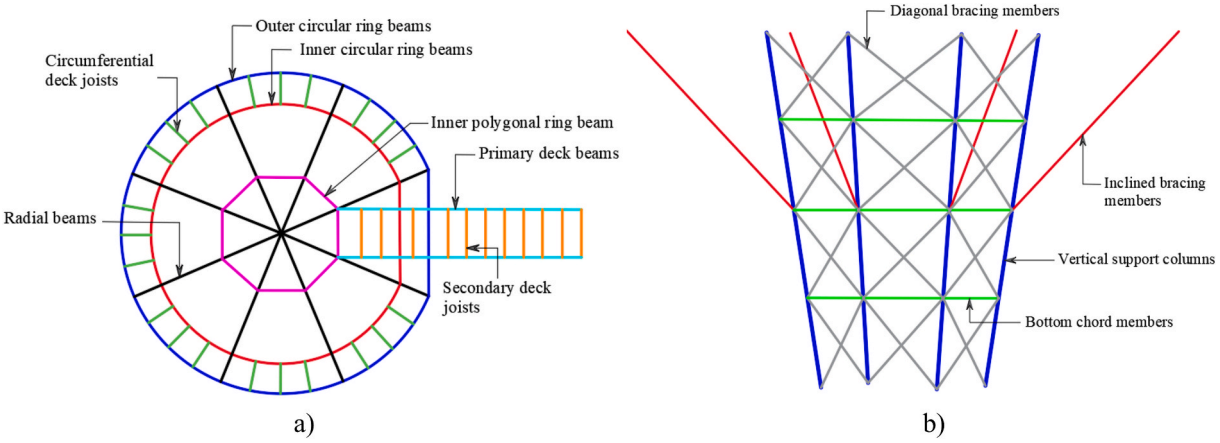

Fig. 5. Structural-component classification: (a) plan view of the deck system and (b) elevation of the lattice-type supporting system.

Table 1
Structural member types and corresponding cross-sectional properties used in the model.

Structural System	Material	*Element type*	*Section Type*	*Section Name*
Superstructure	S275JR	Outer circular ring beams Inner circular ring beams Circumferential deck joists Radial beams Inner polygonal ring beam Primary deck beamsSecondary deck joists	Wide flange(H-section)	HE400B HE400B HE400B HE500B HE400B HE500BHE300A
Substructure	S235JR	Diagonal bracing members Vertical support columns Inclined bracing memberBottom chord members	Circular hollow section (CHS)	CHS168.3 × 5 CHS339.7 × 12 CHS244.5 × 10 CHS168.3 × 5

develop and compare alternative placement, sizing, and optimisation algorithms.

2. Structural System and Numerical Modelling

2.1. Description of structural system

The structure investigated in this study is the Oylat GOP, located in Hilmiye Village within the İnegöl district of Bursa Province, Türkiye. Its location is shown in Fig. 3. The facility includes an observation platform with an approximate area of 250 m^2, together with a cafeteria, pedestrian walkways, and associated social-use areas. The platform is situated on a rocky hilltop and functions as a tourist attraction offering panoramic views of the surrounding landscape. Its elevated topographic position, slender supporting system, and irregular deck geometry make it a relevant case study for detailed structural and dynamic assessment.

From a structural perspective, the facility is separated into three dynamically relevant subsystems: the circular ring–radial deck, the tapered spatial lattice tower, and the inclined access ramp (Fig. 4). This subdivision is used throughout the numerical model and retrofit discussion because the damper layouts act differently on the tower–support and deck load paths. Fig. 5 identifies the member groups used in the detailed load-transfer description below.

The platform has a circular deck and a straight access deck (Fig. 5**a**). The circular deck contains outer and inner ring beams. Radial beams connect the centre region to the perimeter. An inner polygonal ring provides an intermediate load path and improves continuity. Secondary members support the glass panels and transfer their weight to the main steel framing. The deck is connected to a three-dimensional supporting tower. This arrangement creates several load paths and makes the deck sensitive to torsion and local distortion. A three-dimensional lattice

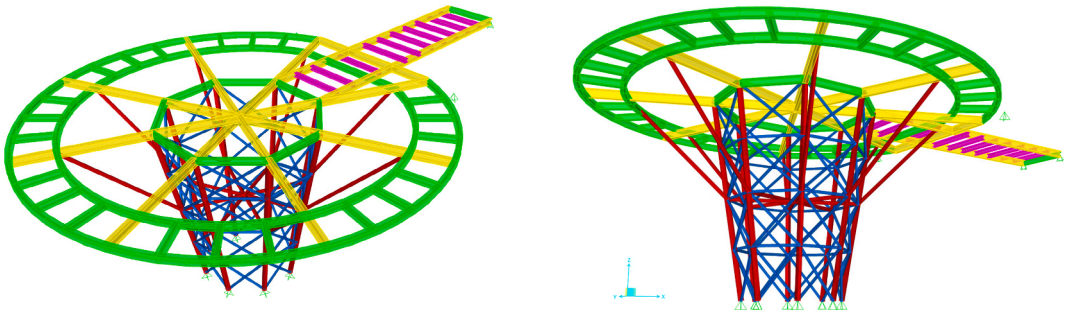

Fig. 6. Three-dimensional SAP2000 model of the Oylat GOP.

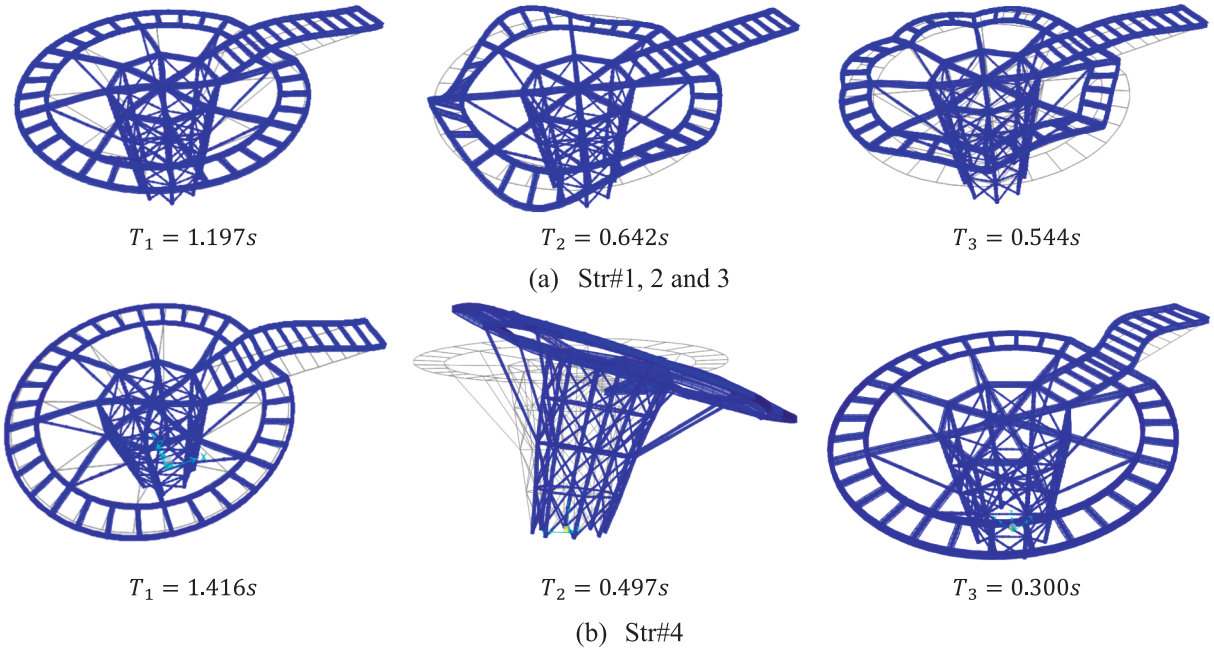

Fig. 7. First three mode shapes and natural periods for (a) Str#1–Str#3 and (b) Str#4.

tower supports the platform (Fig. 5**b**). Its columns incline outward and form a truncated cone. Triangulated braces connect the columns. The wider base improves global stability. The inclined columns carry vertical loads and also resist lateral response together with the braces. The access ramp provides another connection to the surrounding rock. The tower, deck, and ramp therefore interact during earthquake excitation.

2.2. Numerical modelling

A three-dimensional structural model of the GOP was developed in SAP2000 [50]. For computational efficiency, SAP2000 was coupled with MATLAB through its Open Application Programming Interface (OAPI) to automate repeated model updates, analysis execution, and result extraction. This coupling is an implementation tool and is not presented as a methodological contribution. The tower, circular deck, and access ramp were represented by three-dimensional frame elements. The lower supporting system was assigned S235JR steel and the upper deck system S275JR steel. The glass panels were not represented as stiffness-contributing shell or diaphragm elements; their weight was applied to the supporting beams and included through the defined mass source. The tower-base and ramp-end supports restrained U1, U2, and U3 while releasing R1, R2, and R3, thereby representing idealised pinned support conditions. Frame-end releases were assigned to 176 members, predominantly for local M2 and M3, with torsional release at selected ends; members without releases retained full frame continuity. No rigid diaphragm, body, or equal constraint was assigned to the circular deck. The material grades, member groups, and assigned sections are summarised in Table 1.

The structural mass source included self-weight and the relevant superimposed load contributions. Gravity and earthquake response-history cases were evaluated separately. The response-history cases started from an unstressed state and did not include a gravity-preloaded initial condition. Consequently, gravity-induced geometric stiffness was not carried into those cases; the activated P–Delta option acted only on forces developed within the response-history analysis. The reported D/C ratios are therefore seismic-only comparative indices rather than final combined gravity-plus-earthquake code checks. Large-displacement and material nonlinearity were not activated. The adopted model is suitable for comparative elastic demand assessment but does not simulate yielding, cyclic deterioration, fracture, local buckling, or collapse. The resulting three-dimensional numerical model is shown in Fig. 6. No field-vibration data were available for this study; accordingly, the numerical model was not experimentally calibrated and is used here only as a comparative elastic proof-of-concept model.

2.3. Modal characteristics of the structure

Fig. 7 shows how the hybrid intervention changes global and local deformation. The first three periods of the unstrengthened configurations are 1.197, 0.642, and 0.544 s. For Str#4, they are 1.416, 0.497,

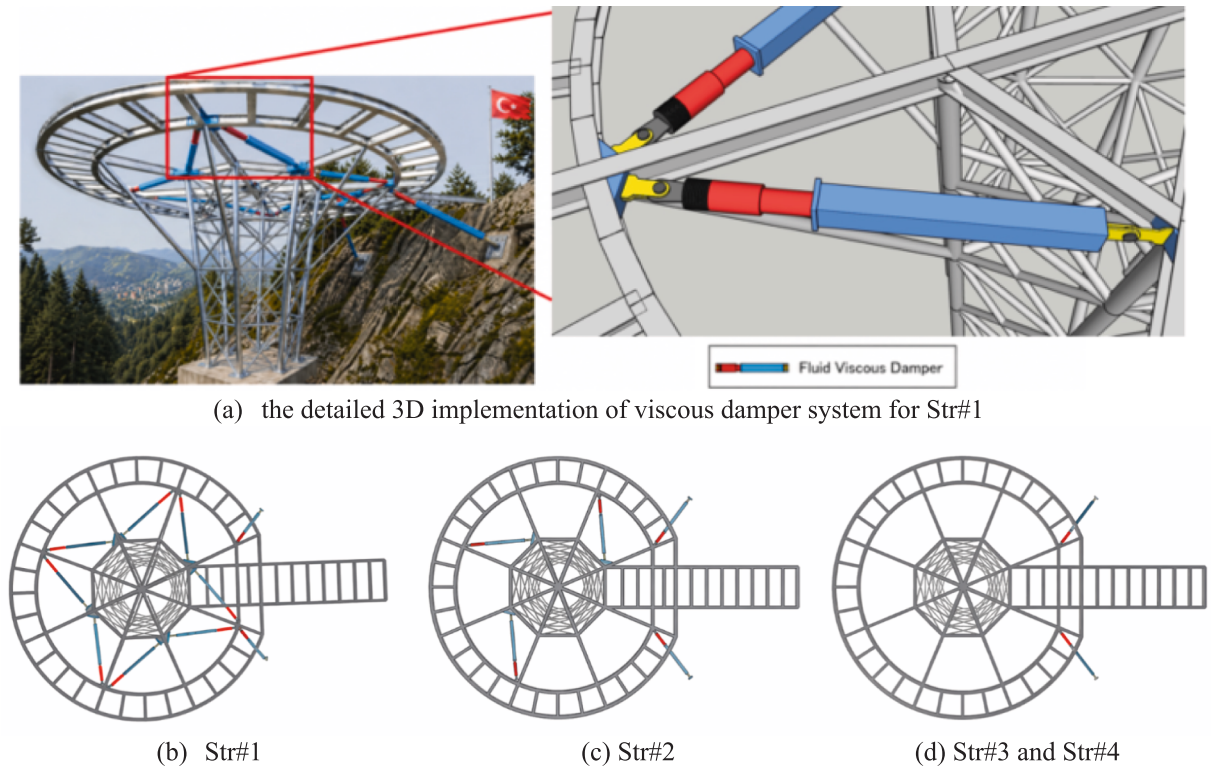

Fig. 8. Conceptual damper installation and idealised force-transfer layouts for Str#1–Str#4. In (a), the deck-side steel attachment plate is welded to the deck beam. The arrangements indicate device orientation and load-path intent only and do not represent final connection, fabrication, or anchorage design.

and 0.300 s. The first mode remains a global torsion-coupled mode. Its RZ participation increases from about 82.65% to 84.82%. The longer first-mode period does not mean that local stiffness decreases. The side plates increase the local ring-beam stiffness. They also increase deck mass and peripheral polar inertia. This change in the generalised mass-to-stiffness balance helps explain the longer first period. The shorter second and third periods show that the local deck-distortion and torsion-sensitive higher modes become stiffer. The first 30 Ritz vectors capture about 96.99% of UX mass, 99.49% of UY mass, and 91.21% of RZ mass in the unstrengthened configurations. The corresponding Str#4 values are 98.84%, 99.89%, and 95.75%.

2.4. Member capacity assessment and comparison criterion

Member capacity indices were obtained in SAP2000 using the AISC 360-10 LRFD steel-design module [51] with the Direct Analysis Method, General Second-Order effects, and the 'Tau-b fixed' stiffness-reduction option. Gravity and earthquake analyses were performed as separate cases. For the comparison reported in Table 3, each response-history case started from an unstressed state; neither a gravity-prestressed initial condition nor a combined gravity-plus-earthquake design envelope was used. The reported D/C values are therefore seismic-only member-utilisation indices evaluated on a common analytical basis for comparing the retrofit strategies, rather than final construction-design compliance checks. The activated P–Delta option did not substitute for gravity preloading of the initial state.

Member performance was assessed using the SAP2000 AISC LRFD demand-to-capacity ratio. The nominal code acceptance boundary is D/C = 1.00. For the present retrofit comparison, D/C $\leq$ 0.80 was selected before the analyses as a study-specific conservative target that retains a 20% utilisation reserve below the nominal boundary. The value is not prescribed by AISC, derived from a formal reliability calibration, or intended as a universal performance limit. It provides a uniform decision criterion for comparing the four strategies while acknowledging unmodelled uncertainty in connections, material response, and device limits.

2.5. Dynamic analysis procedure and damping definition

The earthquake response was evaluated by direct integration using the Hilber–Hughes–Taylor procedure. Steel members remained linearly elastic, while P–Delta geometric effects were included. The analyses therefore represent response-history analyses with geometric second-order effects rather than material-nonlinear time-history analyses. Thirty Ritz vectors were used for modal characterisation. Structural inherent damping was represented by Rayleigh damping, with the damping matrix defined by Eq. (1). The Ritz vectors were used only for modal characterisation; the direct-integration response was not truncated to those vectors.

$$C = \alpha_M M + \beta_K K \quad (1)$$

In Eq. (1), C, M, and K denote the damping, mass, and stiffness matrices, respectively. The mass- and stiffness-proportional coefficients are $\alpha M = 0.1367$ and $\beta K = 0.002660$. These coefficients correspond to 2% critical damping at the first two periods of the unstrengthened configuration (1.197 and 0.642 s). For each spectrally matched motion, the same E–W acceleration history was applied simultaneously to U1 and U2. The loading therefore represents equal-component, perfectly correlated biaxial excitation with a fixed 45° resultant direction. It captures coupled two-axis structural response but does not reproduce the phase difference, amplitude ratio, cross-correlation, orientation variability, or fault-normal/fault-parallel characteristics of an independent two-component record pair.

2.6. Modelling of viscous dampers (VDs)

The fluid viscous dampers were represented by two-joint Damper–Exponential link elements acting in local U1. A Maxwell represen-

Table 2
Main parameters of the selected ground-motion records.

Record	Earthquake	Station	R_{epi}(km)	R_{rup}(km)	Vs30(m/s)	PGA (cm/s^2)	PGV(cm/s)	PGV/PGA	T_p(s)
S4614 Pazarcık	Pazarcık (Mw 7.7)	S4614	31.42	8.25	541	2178.71	72.15	3.31	3.66
S2718 Pazarcık	Pazarcık (Mw 7.7)	S2718	48.3	2.1	527	644.97	113.16	17.55	3.98
S4614 Elbistan	Elbistan (Mw 7.6)	S4614	37.35	7.09	541	206.05	32.87	15.95	3.68

Note: Repi = epicentral distance; Rrup = rupture distance; Vs30 = average shear-wave velocity in the upper 30 m; PGA = peak ground acceleration; PGV = peak ground velocity; Tp = pulse period.

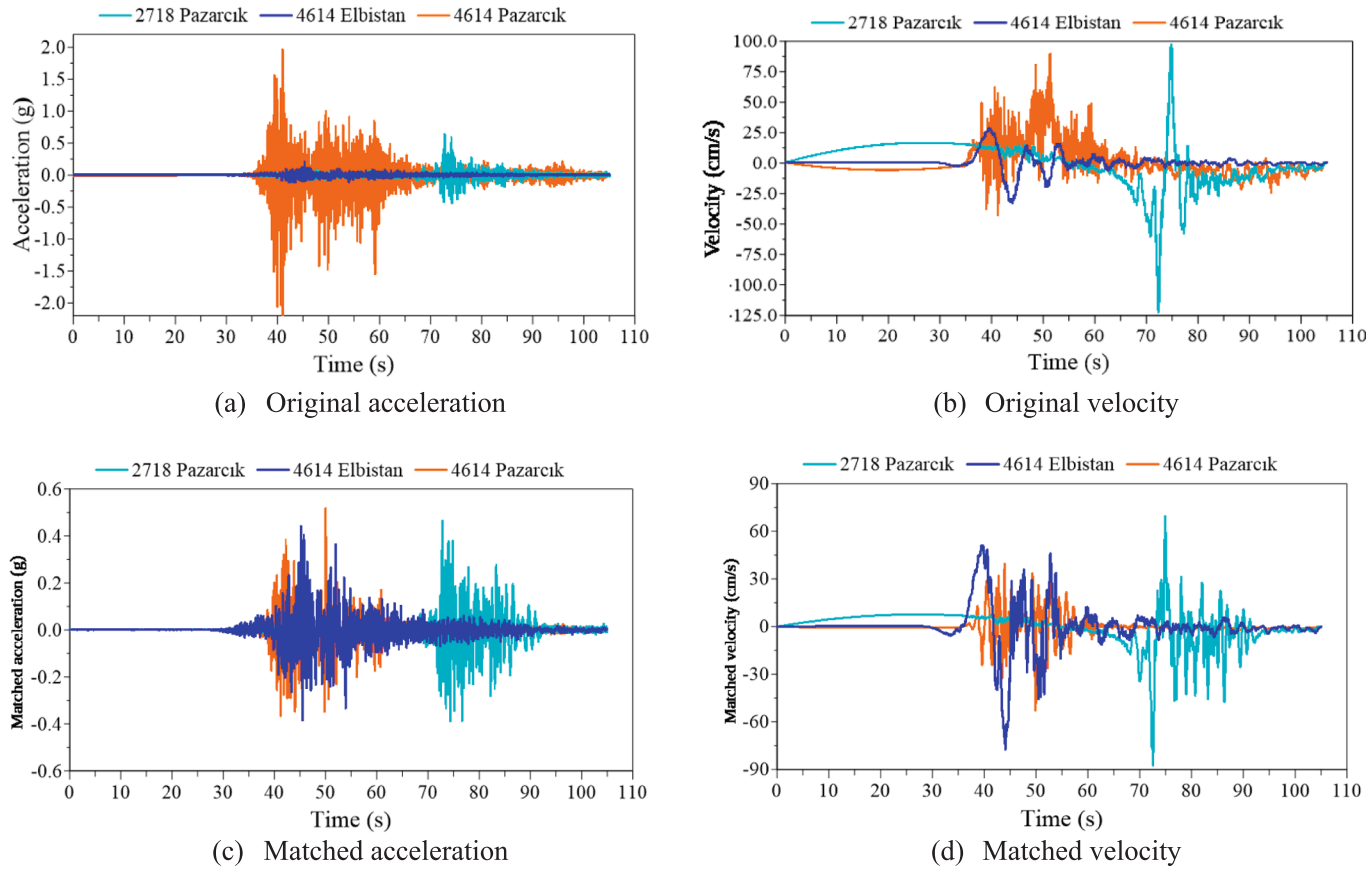

Fig. 9. Acceleration and velocity histories of the selected E–W components: (a, b) original records and (c, d) spectrally matched records.

tation, consisting of a spring and dashpot in series, was used with an axial stiffness of 111,000 kN/m. The adopted constitutive relation is given by Eq. (2).

$$F_d = C_d \mathrm{sgn}(\dot{\delta})|\dot{\delta}|^{\alpha_d} \tag{2}$$

In Eq. (2), F_d is the axial damper force in kN. C_d is the viscous damping coefficient. The symbol $\dot{\delta}$ is the relative velocity between the damper ends in m/s. The term α_d is the velocity exponent, and sgn(·) is the sign function. This study uses $\alpha_d = 1.0$. The force–velocity relation is therefore linear, and C_d has units of kN·s/m. Final product selection must use qualified force, stroke, velocity, temperature, and durability data from the manufacturer [52]. $C_{d,initial}$ must be positive. The link formulation does not represent force saturation, maximum velocity or available stroke, end-stop impact, temperature dependence, leakage, or device failure. The computed link forces and relative displacements are therefore analytical demands, not device-qualification checks. Nonlinear fluid viscous dampers with $0 < \alpha_d < 1$ were not analysed. If such devices are considered, C_d must be recalibrated for the selected α_d because the force–velocity relation changes with the exponent [53–55].

2.7. Damper installation and idealized force-transfer details

The model contains external and internal fluid viscous dampers (FVDs). External devices connect the tower or deck-support system to rock-supported points and primarily control vertical support-column demand. Internal devices act within the circular deck to reduce ring-beam distortion, torsion-sensitive deformation, and residual member demand. Each device is represented by a two-joint axial link aligned with its idealised centreline. The damper-end nodes are therefore idealised force-transfer interfaces, and Fig. 8 shows the intended layout and load path rather than a fabrication detail. At the deck connection in Fig. 8a, the steel attachment plate is welded directly to the deck beam. The damper connects to this attachment through a replaceable clevis-and-pin detail, and the welded plate transfers the reversible axial damper force into the deck framing. The preliminary detail assumes two symmetric continuous fillet joins and aligns the plate as closely as practicable with the damper axis. Short transverse stiffeners or a local diaphragm should distribute the force into the beam web and flanges and limit local distortion. A short component-level check was made for an assumed reversible design action of 200 kN. The 200-kN value is

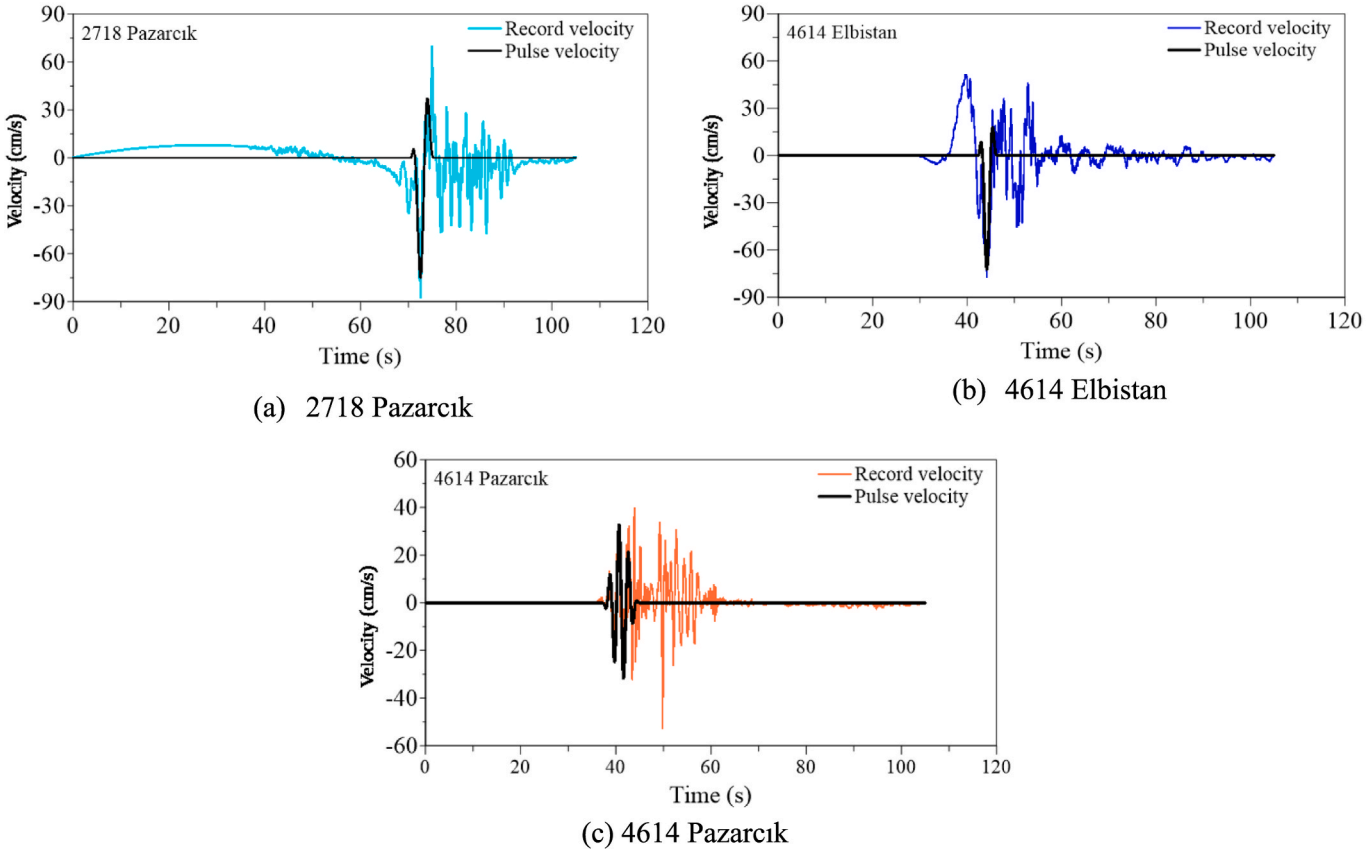

Fig. 10. Original record velocity histories and the extracted pulse components used only for descriptive characterisation before spectral matching.

treated directly as the design action and is not factored again. The attachment plate and deck beam are taken as S275JR steel, with yield and ultimate tensile strengths of 275 and 430 MPa, respectively. For the EN 1993-1-8 fillet-weld check [56], the adopted S275 weld correlation factor and joint partial factor are 0.85 and 1.25, respectively. Two effective weld lengths of 150 mm are assumed, giving a total effective length of 300 mm. For the attachment plate, a preliminary gross-section yielding check was made with a 150-mm plate width and a material partial factor of 1.0 in accordance with EN 1993-1-1 [58].

The preliminary detail therefore adopts a continuous 5-mm effective weld and a 12-mm attachment plate. The corresponding simplified weld and plate resistances are about 351 and 495 kN, respectively, and both exceed 200 kN. These values are screening dimensions, not a complete connection design. Final detailing must use the governing individual-device force, stroke, and velocity envelopes and must verify weld-group eccentricity, reversed-cycle fatigue, plate bending, net-section rupture and block tearing, clevis and pin response, the heat-affected zone, beam web/flange local limit states, stiffeners, weld access and inspection, corrosion protection, and rock anchorage. Fabrication and execution should comply with EN 1090-2 [57]; established gusset-plate response and buckling principles remain relevant to the clevis/gusset portion [59,60].

2.8. Characteristics and spectral matching of the selected near-source ground motions

Three near-source E–W records from the 2023 Kahramanmaraş earthquake sequence were selected. The set supports a controlled, structure-specific comparison. It is not large enough for code-level statistics, probabilistic optimisation, or general damper calibration. Table 2 gives moment magnitude Mw, epicentral distance Repi, closest rupture distance Rrup, V_S30, PGA, PGV, PGV/PGA, and pulse period Tp. The units are shown in the Table. Each E–W component was individually matched in SeismoMatch 2025 [61] to the 5%-damped site-specific TBEC 2018 DD-2 horizontal elastic spectrum. The original E–W records were used as supplied before the spectral-matching step. DD-2 corresponds to a 10% probability of exceedance in 50 years and an approximate 475-year return period. The original and matched spectra are shown together because spectral matching changes the frequency content. Pulse-related descriptors refer to the original records; preservation of the original velocity pulse after matching was not assumed. The arithmetic-mean spectrum is provided only for visual comparison and was not used in the record-specific damper-sizing procedure.

The selected records were matched to the target spectrum using SeismoMatch [61]. Its wavelet-based procedure modifies the acceleration history to reduce spectral mismatch over the specified period range rather than applying a single uniform scale factor. Because these adjustments can alter both time- and frequency-domain characteristics, the matched histories were treated as new analysis inputs and the original pulse descriptors were not assumed to remain unchanged. The implemented procedures follow the wavelet-based formulations of Hancock et al. [62] and Al Atik and Abrahamson [63]. Fig. 9 shows the time histories of the selected motions. The original and matched acceleration histories differ in amplitude concentration and effective duration. Their velocity histories show that the largest excursions occur in short time windows. The matched records provide a common DD-2 spectral-demand basis for comparison. However, spectral matching shifts the frequency content. It does not guarantee that the original pulse amplitude, phase, or waveform is preserved. As this study is just proof of concept, future study should examine the extension of this study under a set of earthquake records.

Fig. 10 presents the descriptive velocity-pulse decomposition of the original E–W records. The decomposition suggests different degrees of pulse concentration, but it is not used as a post-matching pulse

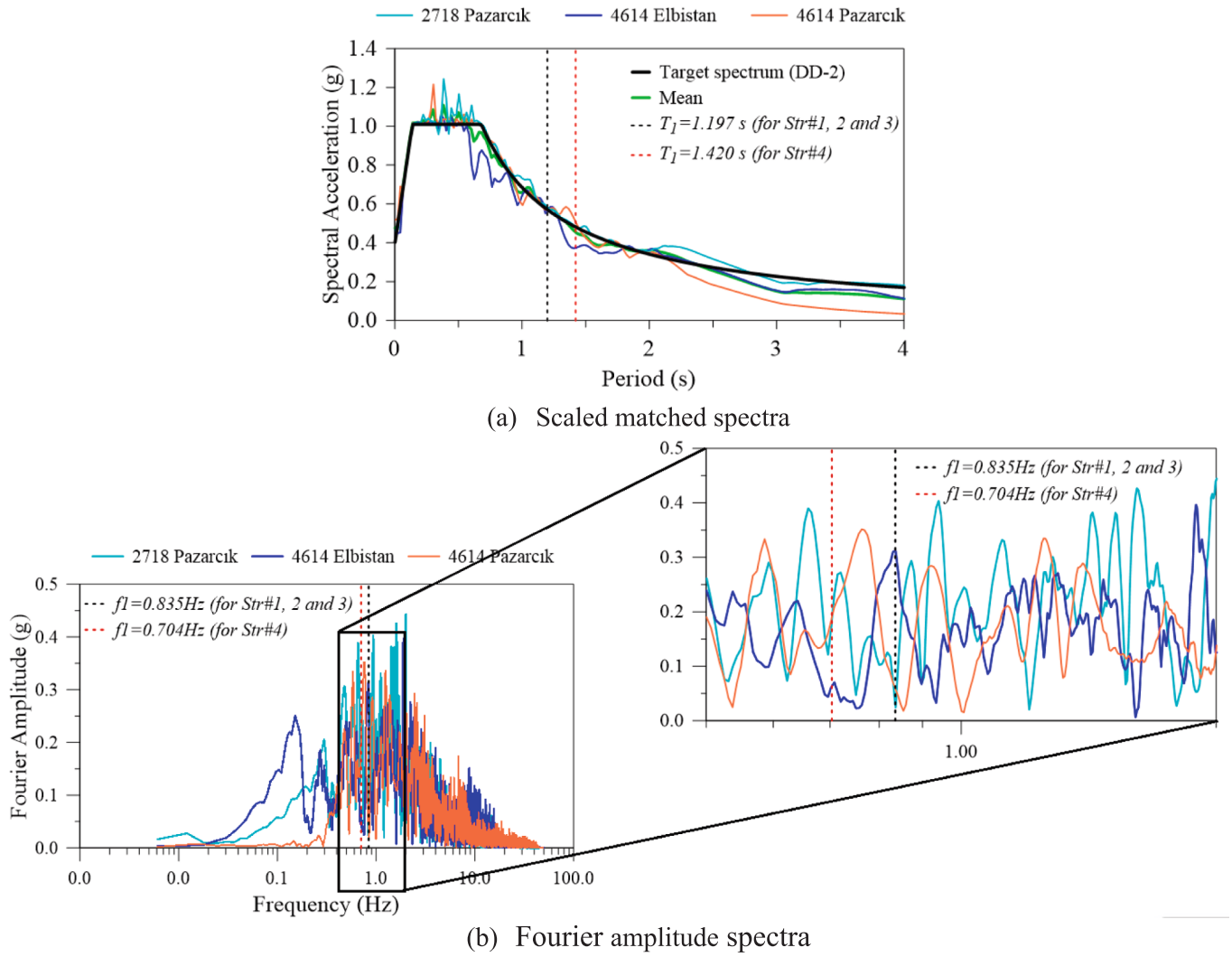

Fig. 11. (a) Original and spectrally matched 5 %-damped response spectra compared with the site-specific DD-2 target spectrum; (b) Fourier amplitude spectra of the matched E–W records.

classification. Because the motions were subsequently modified by spectral matching, the original pulse amplitude, phase, period, and waveform cannot be assumed to remain unchanged. The pulse-related quantities in Table 2 and Fig. 10 are therefore reported only as original-record descriptors and are not used as acceptance criteria in the damper-sizing procedure.

The Fourier spectra contain non-negligible amplitudes near the first-mode frequencies of approximately 0.835 Hz for the unstrengthened configurations and 0.706 Hz for Str#4. This indicates that the matched records contain frequency components capable of exciting the global modes, but it does not independently establish predominant-frequency coincidence or resonance. The original pulse periods, approximately 3.66–3.98 s, remain substantially longer than the first-mode periods of both structural configurations. The corresponding response and Fourier spectra are presented in Fig. 11.

3. Design Methodologies and Retrofitting Strategies

3.1. Design methodology I (DM-I): performance assessment framework

DM-I provides a preliminary screening framework for determining whether the undamped model satisfies the adopted member-level target under every selected DD-2-compatible motion. For each record, the maximum D/C ratio is extracted from the complete assessed deck and supporting-system member set. Retrofit is not required only when the record-specific maximum remains at or below the study-specific target for every selected motion. The target D/C $\leq$ 0.80 is a conservative study-specific comparison criterion, not a code-prescribed performance limit. The workflow is shown in Fig. 12 and is implemented as follows:

The flowchart summarises the preliminary screening procedure applied to the bare model before DM-II. The procedure is performed separately for every selected ground-motion record. Its purpose is to determine whether supplemental damping is required.

Set the member-level target. A study-specific member-level target of D/C $\leq$ 0.80 is defined before the analyses. The same target is applied to the complete audited set of deck and supporting-system members. It is a conservative comparison target and not a code-prescribed acceptance limit.

Run record-specific response-history analyses. Each selected ground-motion record is analysed separately. For a given record, the spectrally matched input is applied simultaneously in the two horizontal directions, in accordance with the adopted input definition. Direct-integration response-history analysis is then performed using the predefined model settings.

Find the maximum member D/C ratio for each record. For each record, the peak D/C ratio is obtained for every audited deck and supporting-system member. The largest of these values is retained as the

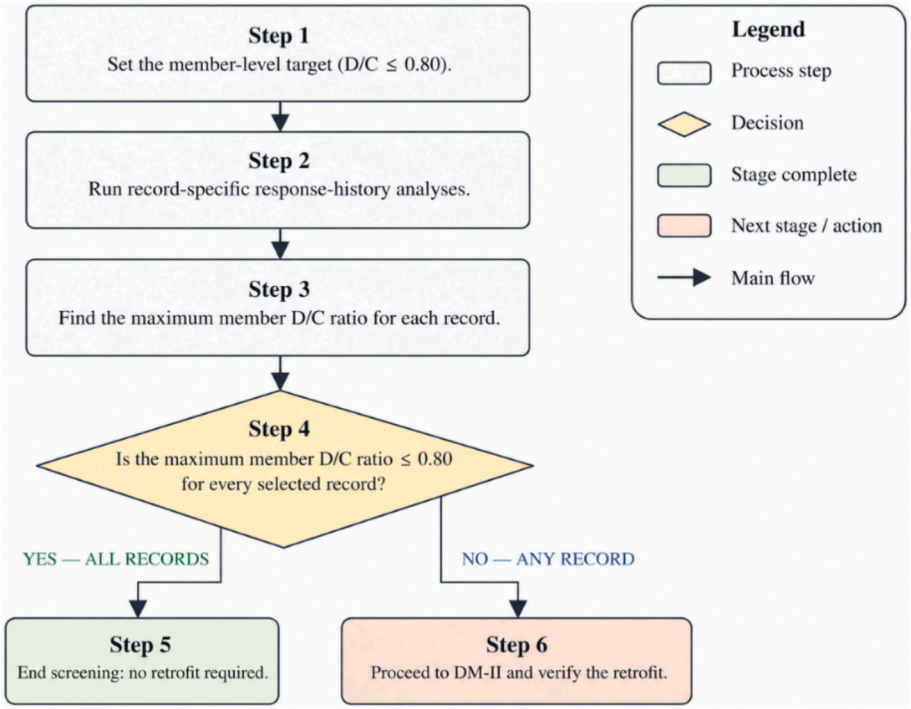

Fig. 12. Design Methodology I (DM-I) screening workflow.

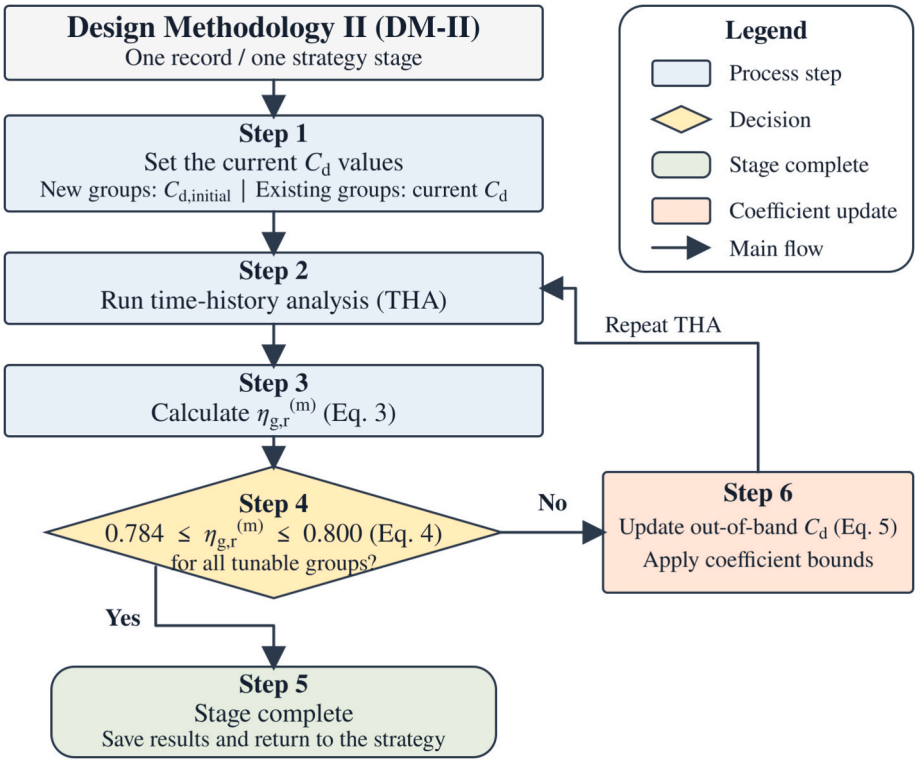

Fig. 13. Simplified DM-II coefficient-sizing loop for one record and one strategy stage.

governing maximum for that record. This approach prevents a local exceedance from being hidden by results from other members.

Check the target for every record. Each record-specific maximum is compared with 0.80. The screening criterion is satisfied only when the maximum member D/C ratio is no greater than 0.80 for every selected record. A mean or median across records is not used for this decision.

End the screening when no retrofit is required. If all record-specific maxima satisfy the target, the screening ends and no retrofit is introduced. This conclusion applies only to the selected records, the

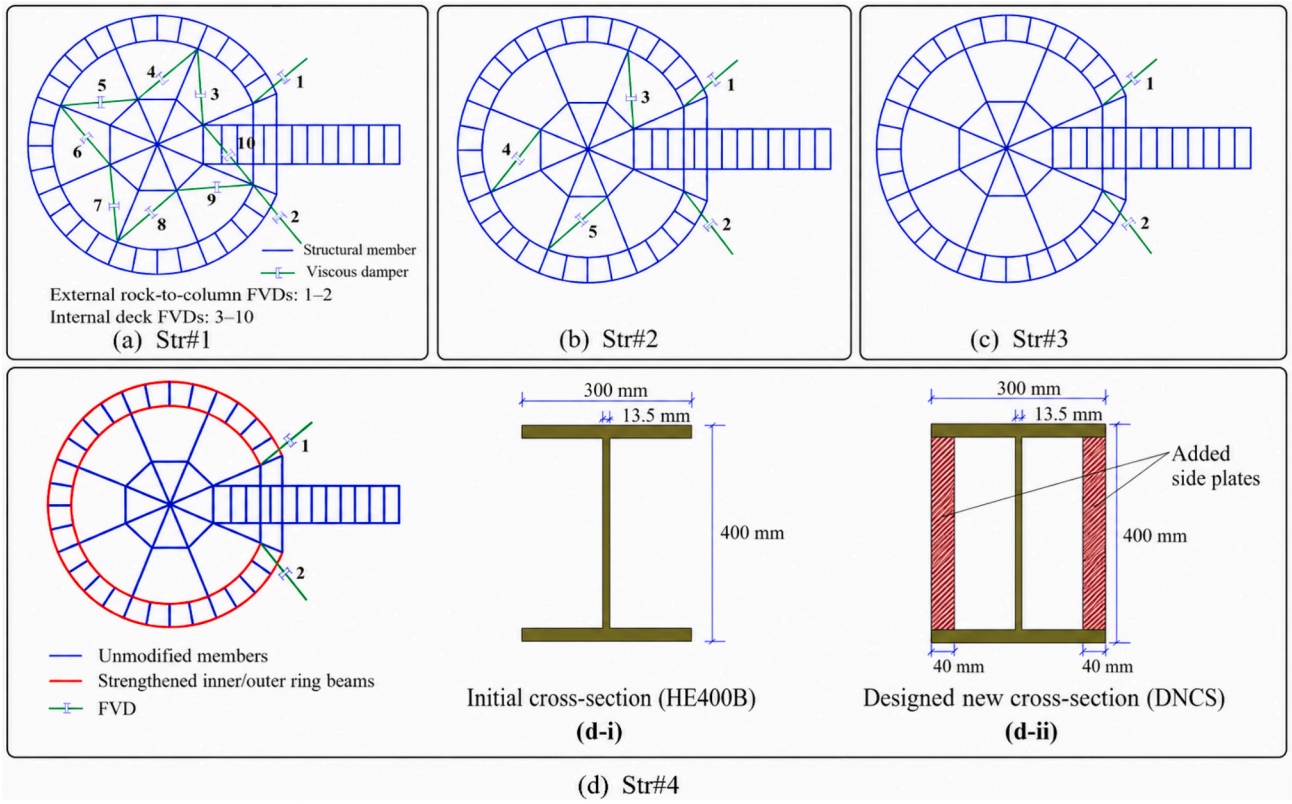

Fig. 14. Physical retrofit layouts for Str#1–Str#4 and the designed new cross-section (DNCS) used in Str#4.

adopted model, and the stated assumptions. It does not represent a general certification of the structure.

Proceed to DM-II when the target is exceeded. If any selected record produces a maximum D/C ratio above 0.80, the procedure continues to DM-II. DM-II tunes the coefficients of the active fluid viscous damper groups within the selected strategy. The final across-record retrofit configuration is then reanalysed under every record, and the relevant members are checked again.

3.2. Design methodology II: iterative damper-sizing procedure

Design Methodology II (DM-II) sizes the active damper groups by iteration. It is applied to one ground-motion record and one strategy stage at a time. At the start of a stage, the strategy identifies the installed groups, the groups that may change, and the member region controlled by each tunable group. A new group starts from Cd,initial. An existing group starts from its current Cd. In Eqs. (3)–(5), *e* denotes a structural member, g denotes the damper group, *r* the record, and m the iteration. The term $Cd,g,r^{(m)}$ is the coefficient of group g for record *r* at iteration m. Each THA gives the D/C ratio for every monitored member. The set Ωg contains the members controlled by group g. Eq. (3) selects the largest D/C ratio in this set. This value is the regional response index $\eta_{g,r}^{(m)}$.

$$\eta_{g,r}^{(m)} = \max_{e\in\Omega_g}[(D/C)_{e,r}^{(m)}] \tag{3}$$

The target response index η_{target} is 0.80. Eq. (4) defines a sizing band from 0.784 to 0.800. The lower limit is 98% of the target. It is only an iteration tolerance. It is not a second structural target. For Str#1, Str#2, and Str#4, the final requirement remains D/C ≤ 0.80 for every audited member under every record.

$$0.784 \le \eta_{g,r}^{(m)} \le 0.800 \tag{4}$$

Eq. (5) updates only a tunable coefficient whose response index is outside the band. If $\eta_{g,r}^{(m)} > 0.800$, C_d increases. If $\eta_{g,r}^{(m)} < 0.784$, C_d decreases. All out-of-band groups are updated from the same THA results. The coefficient bounds are applied after the update. In-band groups and groups fixed by the strategy do not change during that iteration.

$$C_{d,g,r}^{(m+1)} = C_{d,g,r}^{(m)} \times \left(\frac{\eta_{g,r}^{(m)}}{\eta_{target}}\right) \tag{5}$$

Repeat the THA until every tunable group is inside the Eq. (4) band. Then save the stage coefficients and the force, stroke, and velocity demand of each installed device. Return these results to the strategy logic. If the strategy activates a new group, only that group receives Cd,initial. Existing groups keep their current Cd values as the starting values for the next stage. Cd,initial is a bounded numerical seed, not an acceptance condition or an optimal coefficient. The implementation rejects a non-positive or out-of-bounds value before the first THA. The seed may change the iteration path; starting-value independence is not claimed. A stage ends only after THA places every tunable index within 0.784–0.800. If an index is below 0.784, Eq. (5) reduces Cd. if it exceeds 0.800, Eq. (5) increases Cd. THA is repeated after each update. A bound, stagnation, or iteration-limit failure before Eq. (4) is satisfied is reported as non-convergence, and the stage is not accepted.

Fig. 13 summarizes the coefficient-sizing loop for one record and one strategy stage. When a stage converges, its results return to the strategy logic. The strategy may then keep the current layout, activate a new group, retune an existing group, or introduce section strengthening. The complete strategy is run independently for every record. The final design combines the record-specific requirements and is reanalysed under every record. Section 3.3 gives the strategy-specific decisions.

Step 1. Define the current record and strategy stage. Identify the installed groups, the tunable groups, the fixed groups, and the member region controlled by each tunable group. Assign $C_{d,initial}$ only

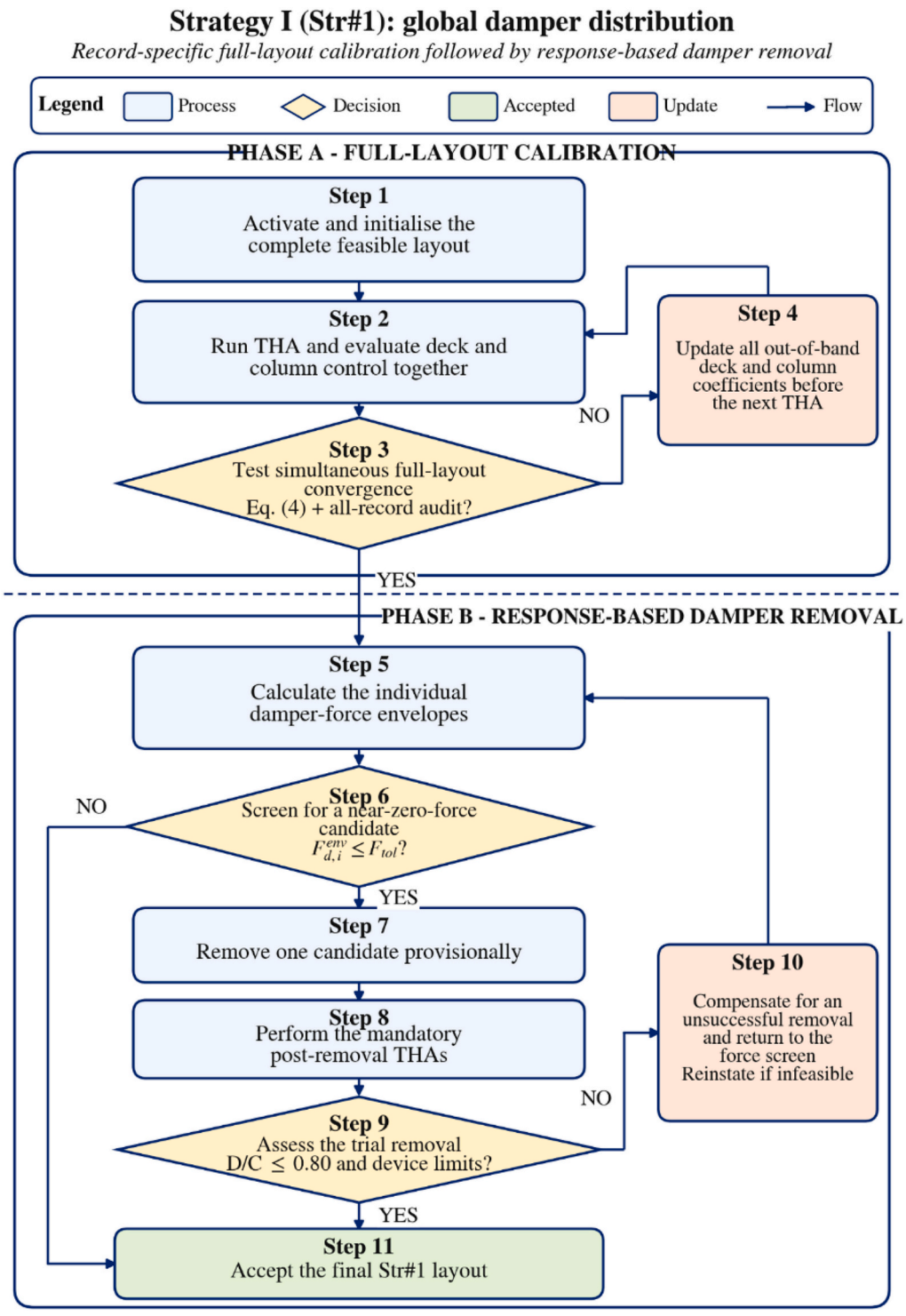

Fig. 15. Strategy I (Str#1): full-layout calibration, response-based near-zero-force damper removal, and post-removal verification.

to a newly activated group. Use the current C_d as the starting value for every existing group.

Step 2. Run the time-history analysis (THA) with the current damper coefficients. Obtain the D/C ratio of every monitored member and the force, stroke, and velocity demand of every installed device.

Step 3. For each tunable group, use Eq. (3) to calculate $\eta_{g,r}^{(m)}$. This is the maximum member D/C ratio in the region controlled by that group.

Step 4. Check Eq. (4) for every tunable group. The stage satisfies the sizing condition only when every $\eta_{g,r}^{(m)}$ is between 0.784 and 0.800.

Step 5. If all tunable groups satisfy Eq. (4), the stage is complete. Save the converged coefficients and the individual-device demands. Return the stage result to the strategy logic.

Step 6. If any tunable group is outside the band, update only its C_d using Eq. (5). Apply the coefficient bounds. Keep the in-band and fixed coefficients unchanged. Return to Step 2 and repeat the THA.

3.3. Retrofitting Strategies

The four strategies use the same model but apply different

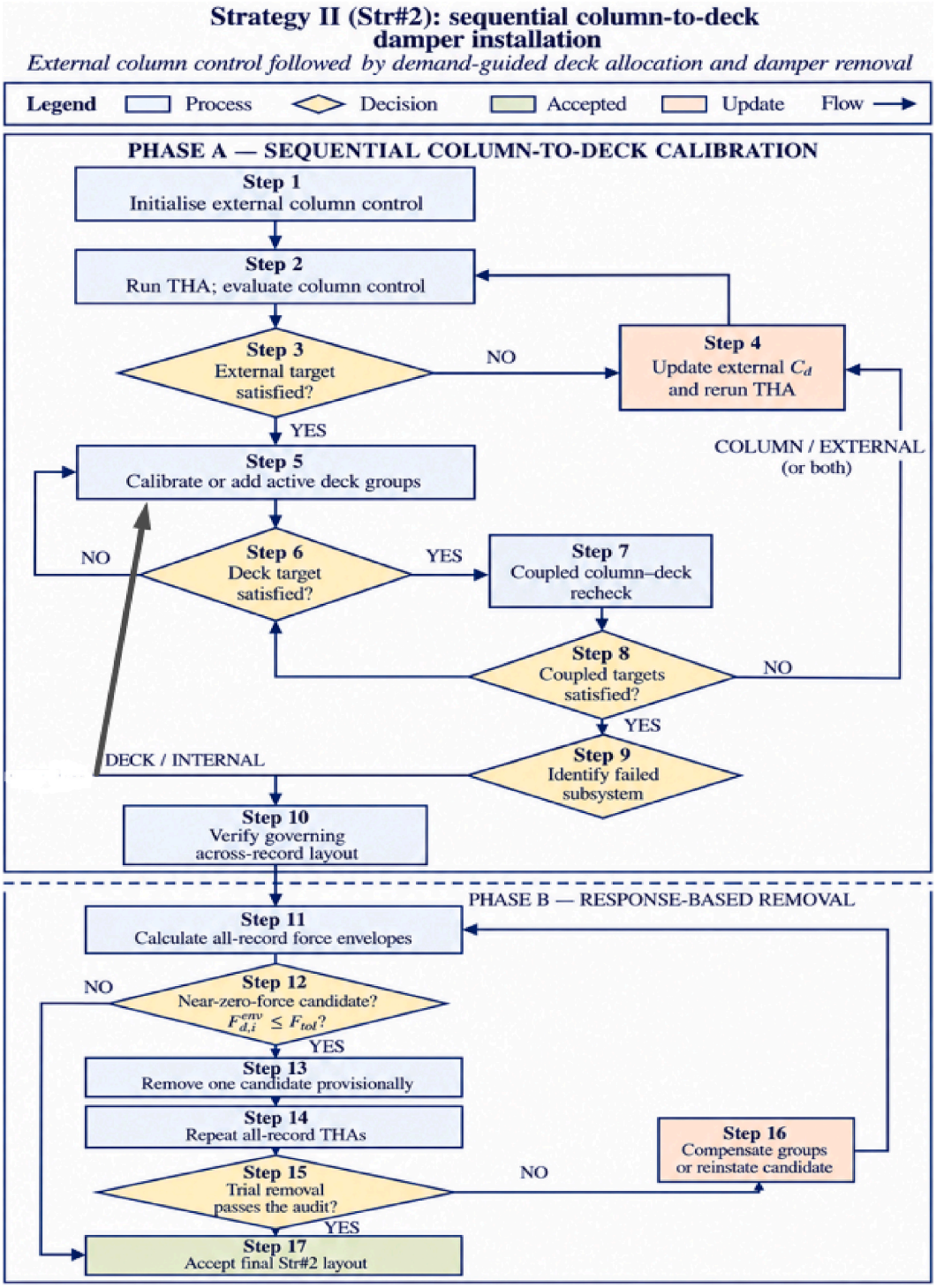

Fig. 16. Strategy II (Str#2): external column-control calibration, sequential demand-guided deck allocation, coupled verification, and response-based removal of corner and deck dampers.

interventions. Str#1 activates and tunes the full deck-and-support damper layout at the same time. Str#2 controls the columns first. It then keeps the external coefficient unchanged while adding internal deck dampers one at a time. After each addition, the internal groups are checked and retuned if needed. The columns are checked again after the deck target is met. Str#3 uses only the external dampers and intentionally leaves the deck untreated. Str#4 also begins with external column control, but it strengthens the ring beams instead of adding internal deck dampers. This comparison shows how the order and type of intervention affect the structural response. The Section 3.2 safeguards apply to every tunable group. Fig. 14 shows the physical retrofit layouts. Str#1 uses all feasible external and internal FVD locations, numbered 1–10. Str#2 uses external locations 1 and 2. It also uses internal locations 3–5, which were selected by the sequential demand procedure. Str#3 uses only external locations 1 and 2. Str#4 also uses only these two external FVDs. Its deck intervention is the designed new cross-section shown in Fig. 14**d.** This section adds side plates to the inner and outer HE400B ring beams.

The four strategies therefore retain distinct comparison objectives while using a consistent verification hierarchy. Str#1 calibrates the full layout concurrently; Str#2 calibrates the external group first and then adds internal deck devices sequentially; Str#3 remains an external-only column-control benchmark; and Str#4 combines external damping with deck strengthening. Response-based removal is considered only after the governing across-record configuration has passed its primary audit. The candidate pool contains all active devices in Str#1, external and internal devices in Str#2, and only external corner devices in Str#4. In every applicable strategy, removal is accepted only after the reduced configuration has been reanalysed under all records and the complete member and device-demand criteria remain satisfied.

3.3.1. Strategy I (Str#1): global damper distribution

Strategy I (Str#1) is the simultaneous full-layout damping benchmark. At the outset, FVDs are installed at every technically feasible deck location shown in Fig. 14, including the ring-radial framing regions. External corner FVDs are also installed between rock-supported anchorage points and the corresponding ends of the vertical support columns. The internal devices control deck deformation and torsion-sensitive member demand, whereas the external devices reduce demand in the column-control region. All devices are active from the first analysis, and every newly activated damper group is assigned a positive, bounded $C_{d,initial}$. Because the deck and supporting tower are dynamically coupled, the deck- and column-control response indices are obtained from the same time-history analysis (THA) and are updated within one simultaneous feedback loop. Damper removal is excluded until the full layout has converged and the governing across-record configuration has passed the primary audit. Phase A is performed independently for each ground-motion record. Phase B removes only dynamically ineffective devices. This response-constrained, one-device-at-a-time pruning is a simple cost-oriented optimisation surrogate that reduces unnecessary devices and connections; it is not presented as a formal global-cost optimum.

The Str#1-specific implementation is summarized in Fig. 15 and below; each step is applied together with the common DM-II rules and safeguards given in Section 3.2.

Step 1. *Activate and initialise the complete feasible layout.* For the current record, activate every feasible internal deck FVD and every external rock-to-column FVD assigned to Str#1. Assign $C_{d,initial}$ to each newly activated group. This value is only a bounded numerical seed; it is not a convergence or acceptance condition. No device is screened for removal during Phase A.

Step 2. *Run THA and evaluate deck and column control together.* Perform the bidirectional direct-integration THA using the current coefficient vector. From this single analysis state, use Eq. (3) to calculate $\eta_{g,r}^{(m)}$ for every tunable deck-control group and for the external column-control group. Examine the complete member set and store the force, stroke, and velocity demand of every active FVD.

Step 3. *Test simultaneous full-layout convergence.* Verify $0.784 \leq \eta_{g,r}^{(m)} \leq 0.800$ for every tunable deck and column group. The current record-specific stage converges only when all groups satisfy Eq. (4); if any group is outside the band, proceed to Step 4. Repeat Steps 1-4 independently for every record. After all record-specific loops converge, assign the largest required record-specific coefficient at each active location or group and reanalyse the resulting common configuration under every record. Phase B may begin only after every audited member satisfies $D/C \leq 0.80$ and every retained device passes the adopted demand checks under the complete record set.

Step 4. *Update all out-of-band deck and column coefficients before the next THA.* Using the response indices obtained in Step 2, update every out-of-band $C_{d,g,r}^{(m)}$ simultaneously using Eq. (5). Increase the coefficient when the corresponding index exceeds 0.800 and reduce it when the index is below 0.784. Keep in-band coefficients unchanged, enforce the adopted coefficient bounds, and return to Step 2. An update alone cannot be accepted; convergence must be confirmed by a new THA.

Step 5. *Calculate the individual damper-force envelopes.* For the verified common layout, calculate $F_{d,i}^{env}$ for every active damper over all analysis times and selected records. Repeat this calculation whenever Step 10 changes the coefficient vector and returns the procedure to the force screen.

Step 6. *Screen for a near-zero-force candidate.* Check whether any active damper satisfies $F_{d,i}^{env} \leq F_{tol}$. If none does, proceed to Step 11. If several devices qualify, select only the one with the smallest envelope and proceed to Step 7.

Step 7. *Remove one candidate provisionally.* Deactivate only the selected lowest-force device and retain all remaining C_d values unchanged. Removing one device at a time isolates its structural influence and avoids conflating the effects of simultaneous removals.

Step 8. *Perform the mandatory post-removal THAs.* Reanalyze every selected record using the reduced layout and unchanged coefficients. Recheck the complete audited member set and update the force, stroke, and velocity demands of all retained devices.

Step 9. *Assess the trial removal.* If every audited member satisfies $D/C \leq 0.80$ under every record and all retained devices satisfy the adopted practical limits, retain the removal and proceed to Step 11. Otherwise, proceed to Step 10.

Step 10. *Compensate for an unsuccessful removal and return to the force screen.* Keep the candidate inactive and increase the coefficients of the remaining groups associated with target exceedances using Eq. (5). Repeat THA and the complete audit until $D/C \leq 0.80$ is restored for every record; then return to Step 5, rather than accepting the layout directly. If restoration is impossible within the coefficient bounds or device-demand limits, reinstate the candidate, mark it as non-removable for the current configuration, and return to Step 5 with the last feasible layout.

Step 11. *Accept the final Str#1 layout.* Accept the latest verified configuration when Step 6 identifies no eligible active damper or when Step 9 confirms a successful post-removal trial. Save the retained layout, final coefficients, and governing force, stroke, and velocity demands; acceptance requires $D/C \leq 0.80$ for every audited member and every selected record.

3.3.2. Strategy II (Str#2): sequential column-to-deck damper installation

Strategy II (Str#2) uses a demand-guided, sequential column-to-deck allocation so that the complete internal layout is not activated a priori. For each ground-motion record, the external FVD group connecting the rock anchorage to the column ends is activated first and assigned $C_{d,initial}$. Phase B applies the response-based removal audit to both external corner and internal deck FVDs. This one-device-at-a-time procedure is a transparent, cost-oriented pruning surrogate rather than a formal global-cost optimum.

The record-specific calibration, governing-layout assembly, and removal audit shown in Fig. 16 are implemented as follows; the common DM-II bounds and non-convergence safeguards in Section 3.2 apply at every calibration and compensation stage.

Step 1. Activate and initialize the external column-control group. For the current record, activate only the external rock-to-column FVDs and assign a positive, bounded $C_{d,initial}$. No internal deck FVD is active at this stage.

Step 2. Run THA and evaluate external column control. Perform the bidirectional direct-integration THA, calculate $\eta_{g,r}^{(m)}$ for the column-control region using Eq. (3), audit the associated member D/C values, and store the external-device force, stroke, and velocity demands.

Step 3. Test external-group convergence. Verify $0.784 \leq \eta_{g,r}^{(m)} \leq 0.800$ for the external tunable group and confirm the column-member audit. A value above 0.800 indicates insufficient damping and requires an increase in the coefficient; a value below 0.784 indicates an oversized coefficient and requires a decrease. A NO result leads to Step 4, whereas

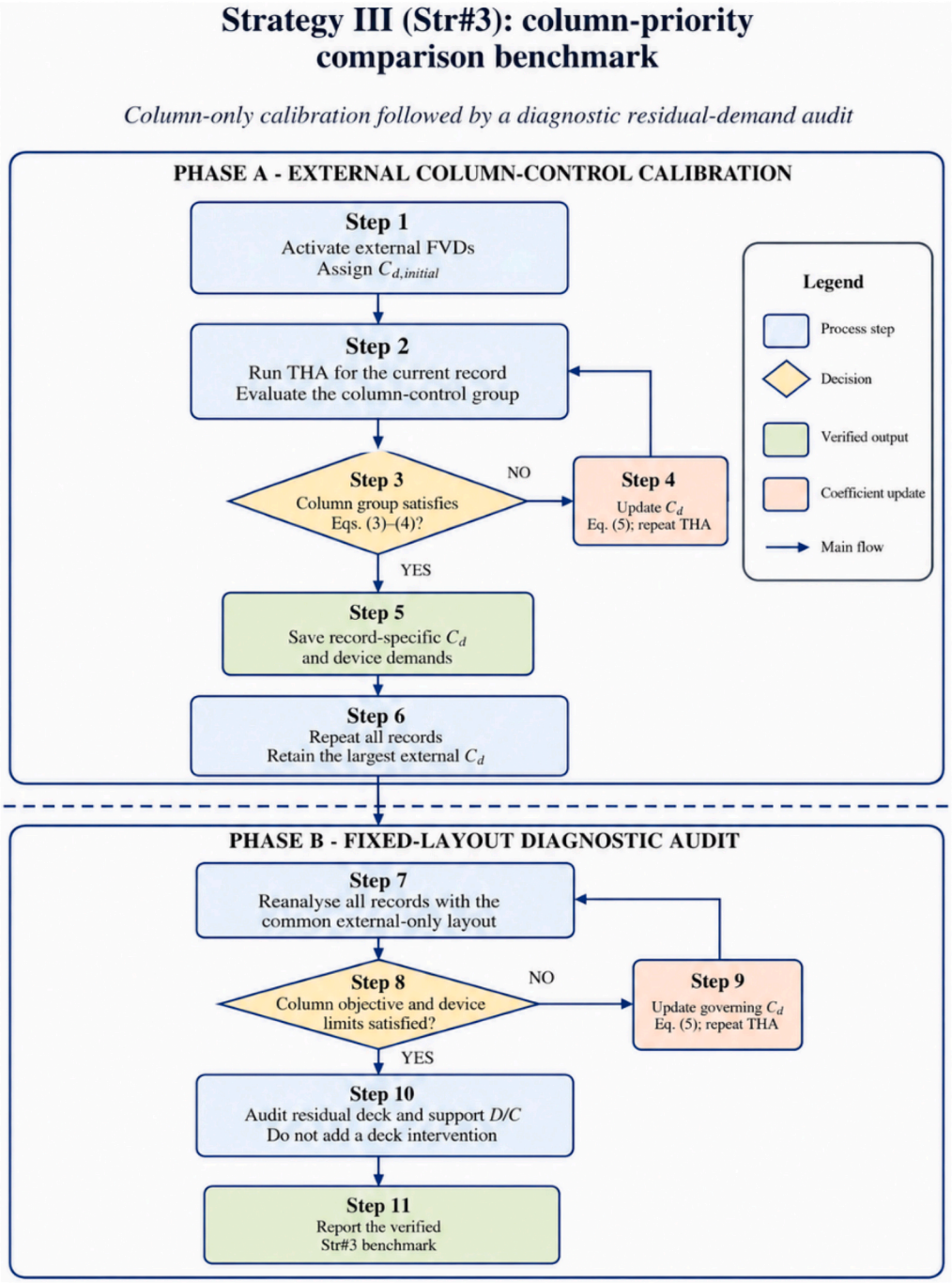

Fig. 17. Strategy III (Str#3): external column-control calibration and fixed-layout diagnostic residual-demand audit.

a YES result leads to Step 5.

Step 4. Update the external coefficient and repeat THA. Update the out-of-band external $C_{d,g,r}^{(m)}$ using Eq. (5) in the direction identified in Step 3, enforce the adopted numerical and device bounds, and return to Step 2. The coefficient-update step cannot be accepted without a new THA.

Step 5. Calibrate active deck groups and add one group only if required. Keep the converged external group active with its coefficient initially fixed. Using the latest THA, re-evaluate every active deck-control group, including all groups installed in earlier cycles, and update all out-of-band internal C_d values simultaneously using Eq. (5). Repeat THA until the active internal groups converge. Then audit the complete deck. If the deck satisfies Eq. (4) and the member-level limit, add no device and proceed to Step 6. If it still fails, select the current highest-demand feasible region not adequately controlled, activate exactly one new internal FVD group there, assign $C_{d,initial}$ only to that group, and repeat the simultaneous calibration of all active deck groups before proceeding to Step 6. Consequently, force redistribution from a new device always triggers a recheck of every earlier active group.

Step 6. Test the complete deck target. Re-audit all deck regions and members after the active internal groups have converged. If any regional maximum remains outside Eq. (4), or any audited deck member has $D/C > 0.80$, return to Step 5 and place the next group at the newly governing feasible region. Proceed to Step 7 only when all deck regions and members satisfy their respective criteria.

Step 7. Perform the coupled column-deck recheck. With all currently active external and internal devices retained, repeat THA and audit the column-control region, all deck-control regions, all relevant members,

and the force, stroke, and velocity limits together. This step captures the redistribution produced by the sequential deck additions.

Step 8. Test the record-specific coupled targets. Accept the current record-specific configuration only when all relevant group indices satisfy Eq. (4), every audited member satisfies $D/C \leq 0.80$, and every active device remains within the adopted practical limits. A YES result leads to Step 10. A NO result leads to Step 9, where the failed control subsystem is identified before the return path is selected.

Step 9. Identify the failed subsystem and select the return path. Use the same coupled-THA results to classify the exceedance as external/column-control, internal/deck-control, or simultaneous. For an external/column-control failure, return to Step 4, update the external coefficient using Eq. (5), and repeat the external THA loop. For a deck-only/internal-control failure, return to Step 5, return all active internal groups together, and add one new group only if the converged active layout remains inadequate. If both subsystems fail, follow the Step 4 path first; after external control reconverges, continue through Step 5. Following either route, Steps 7 and 8 must be repeated, and the layout cannot be accepted directly from an update step.

Step 10. Form and verify the governing across-record layout. Repeat Steps 1-9 for every selected record. Form the common layout from the union of required external and internal locations and assign the largest record-specific C_d at each location. Reanalyse every record and confirm the coupled group, member, and device-limit audits. Save the governing coefficient vector and the independent across-record maxima of force, stroke, and velocity. Phase B begins only after verification.

Step 11. Calculate the corner- and deck-damper force envelopes. For every retained external and internal FVD, calculate $F_{d,i}^{env}$ over all analysis times and selected records. Recalculate the envelopes whenever Step 16 changes the coefficient vector.

Step 12. Screen for a near-zero-force candidate. Using the all-record force envelopes from Step 11, test every retained external corner and internal deck damper against $F_{d,i}^{env} \leq F_{tol}$. If no device satisfies the inequality, proceed to Step 17. If more than one device qualifies, select only the qualifying damper with the smallest envelope for the current trial; all other devices remain active.

Step 13. Remove one candidate provisionally. Deactivate only the selected lowest-force device and keep every remaining C_d value unchanged for the first post-removal analysis. External and internal candidates follow the same one-device-at-a-time rule.

Step 14. Perform the mandatory post-removal THAs. Reanalyse every selected record with the reduced layout. Recompute the relevant group indices and re-audit the complete member set together with the force, stroke, and velocity demands of all retained devices.

Step 15. Assess the trial removal. Retain the removal only if the complete all-record audit is satisfied: the applicable group indices remain within Eq. (4), every audited member has $D/C \leq 0.80$, and all retained devices satisfy their practical limits. A successful trial leads to Step 17; otherwise proceeds to Step 16.

Step 16. Compensate for an unsuccessful removal and return to the force screen. Keep the candidate temporarily inactive and update the affected remaining external and/or internal coefficients using Eq. (5). Repeat the all-record THAs until the audit is restored, then return to Step 11 to recompute the force envelopes. If restoration is infeasible within the coefficient or device-demand bounds, reinstate the candidate, restore the last feasible coefficient vector, mark the device as non-removable, and return to Step 11.

Step 17. Accept the final Str#2 layout. Accept the latest verified configuration when Step 12 finds no eligible device or Step 15 confirms a successful removal. Save the retained external and internal locations, the final C_d values, and the independently governing device-demand envelopes. Final acceptance requires $D/C \leq 0.80$ for every audited member under every selected record.

3.3.3. Strategy III (Str#3): column-priority comparison benchmark

Strategy III (Str#3) is retained as a column-priority comparison benchmark. For each record, only the external rock-to-column FVDs are calibrated; no internal deck damper and no deck-section strengthening is introduced. The external group is updated through the common DM-II loop until the column-control response index satisfies Eq. (4). The converged record-specific coefficient and the individual external-device demands are stored, after which the largest required external coefficient is applied in the common across-record layout.

The common external-only layout is reanalyzed under every selected record. Its column-control objective requires $D/C \leq 0.80$ for the audited column region together with the adopted device-demand limits. The deck and the other supporting members are then examined without intervention, and their residual exceedances are reported diagnostically. Response-based damper removal is intentionally not applied to Str#3 because its fixed external-only arrangement defines the comparison benchmark; pruning that arrangement would change the reference question rather than complete a full-system retrofit.

The Str#3 benchmark is summarized in Fig. 17 andimplemented through the following steps; the common DM-II safeguards in Section 3.2 remain applicable to every external-group update.

Step 1. *Activate and initialize the external group.* For the current record, activate only the external rock-to-column FVDs and assign $C_{d,initial}$.

Step 2. *Run THA and evaluate column control.* Perform THA, evaluate $\eta_{g,r}^{(m)}$ using Eq. (3), audit the column-region D/C values, and store the external-device demands.

Step 3. *Test external-group convergence.* Verify $0.784 \leq \eta_{g,r}^{(m)} \leq 0.800$. A NO result leads to Step 4; a YES result leads to Step 5.

Step 4. *Update the external coefficient and repeat THA.* Update the out-of-band external $C_{d,g,r}^{(m)}$ using Eq. (5), apply the numerical bounds, and return to Step 2.

Step 5. *Save the record-specific external solution.* Store the converged external C_d and the force, stroke, and velocity of each external device. Do not introduce a deck intervention.

Step 6. *Form the common external-only layout.* Repeat Steps 1-5 for every record and retain the largest record-specific external C_d required by any motion.

Step 7. *Reanalyze every selected record.* Apply the common external-only configuration and repeat THA for the complete record set. Update the individual external-device demand envelopes.

Step 8. *Verify the column-control objective.* Confirm $D/C \leq 0.80$ for the audited column-control region under every record and verify the external-device practical limits. A NO result leads to Step 9; a YES result leads to Step 10.

Step 9. *Retune the governing external coefficient.* Update the governing external C_d using Eq. (5), enforce the adopted bounds, and return to Step 7. This step verifies only the Str#3 column objective.

Step 10. *Audit residual deck and support demand.* Keep the verified external configuration unchanged and report the number, location, and magnitude of every residual deck or support-member D/C exceedance. Do not add a deck intervention.

Step 11. *Report the verified Str#3 benchmark.* Save the governing external-device demands and the residual member-demand map. Report Str#3 as a verified column-control benchmark, not as a complete-system retrofit.

3.3.4. Strategy IV (Str#4): hybrid damping and section enhancement

Strategy IV (Str#4) combines external column damping with targeted deck-section enhancement. For each record, the external rock-to-column FVDs are calibrated first through the common DM-II loop. No internal deck FVD is installed. After the external group converges, the complete deck is audited. If the deck target is not met, the governing demand region and its response mechanism are identified, the corresponding ring-beam section is strengthened, and the coupled deck-

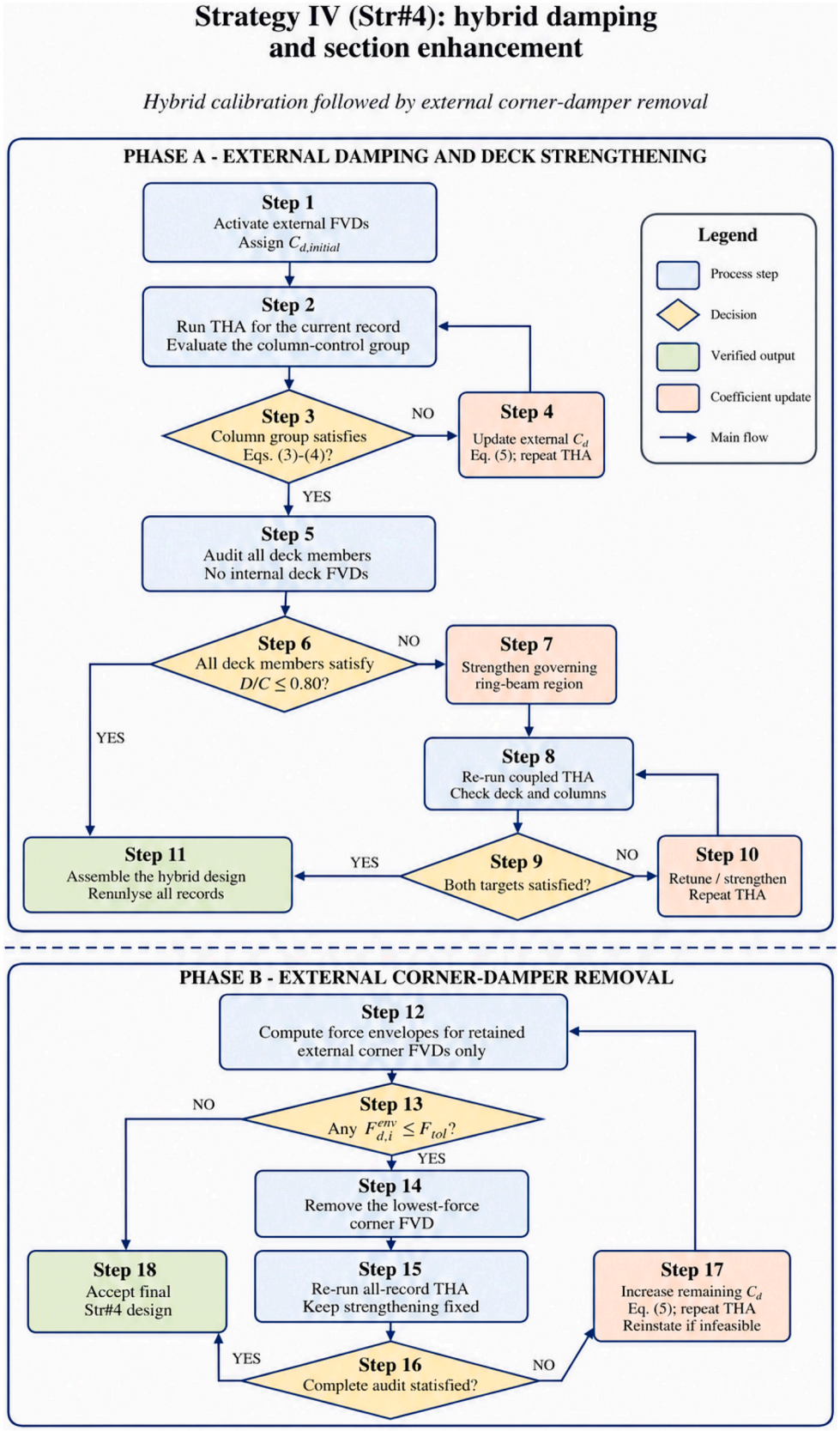

Fig. 18. Strategy IV (Str#4): external damping, deck-section enhancement, response-based corner-damper removal, and post-removal verification.

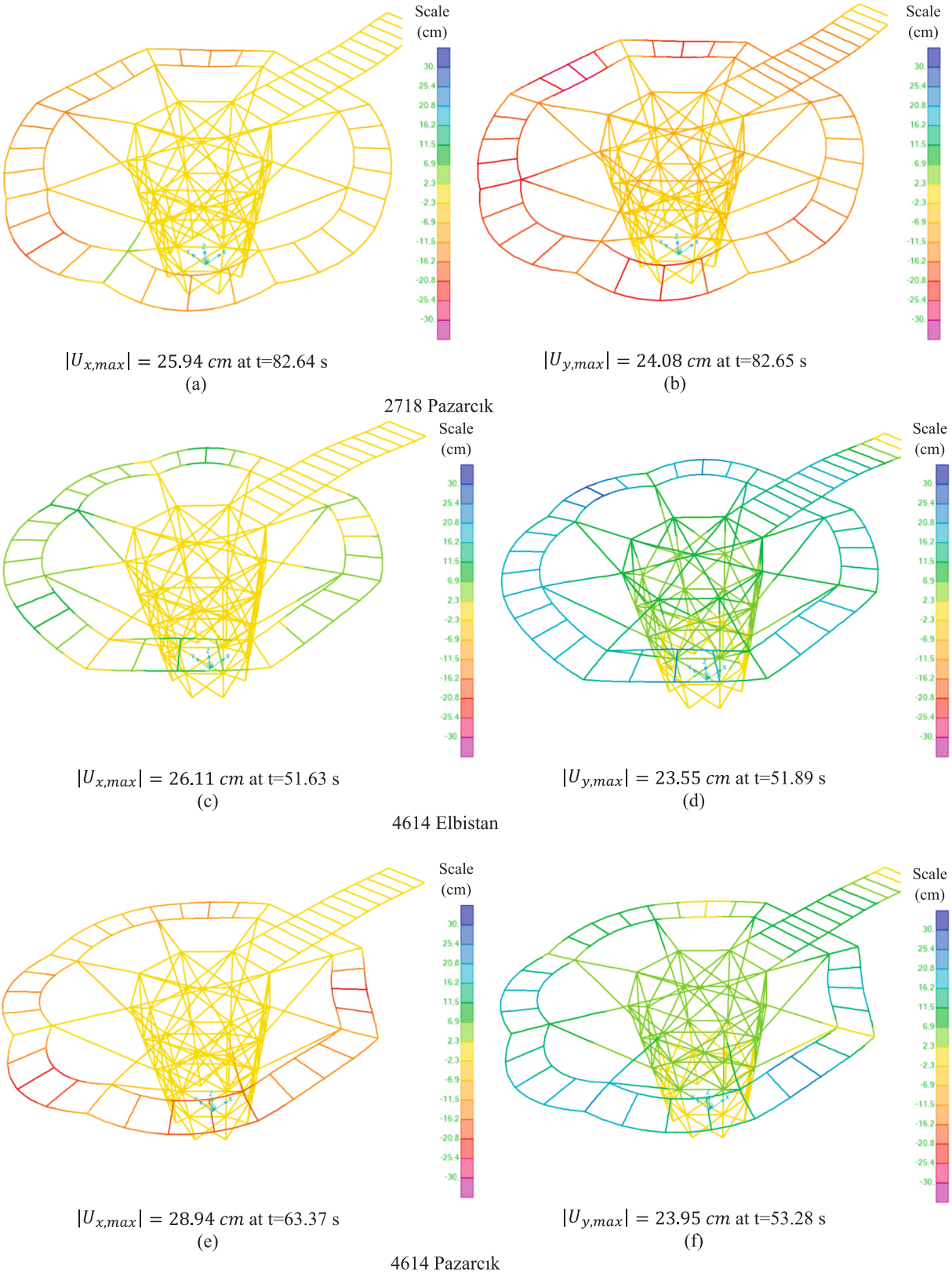

Fig. 19. Contours of maximum horizontal displacement in the U1 and U2 directions (cm) for the bare model under the selected ground motions.

column model is reanalysed. External damping and strengthening are iterated only as required by the two control regions.

Phase A is completed independently for every record. For the Oylat platform, the residual demand was distributed around the torsion-sensitive circular deck rather than confined to one isolated member; the governing solution therefore uses 40-mm side plates on both the inner and outer HE400B ring-beam systems. Each section change is followed by THA because it modifies stiffness, mass, polar inertia, and force transfer. The final hybrid design retains every strengthening region required by any record, uses the largest required extent at each region,

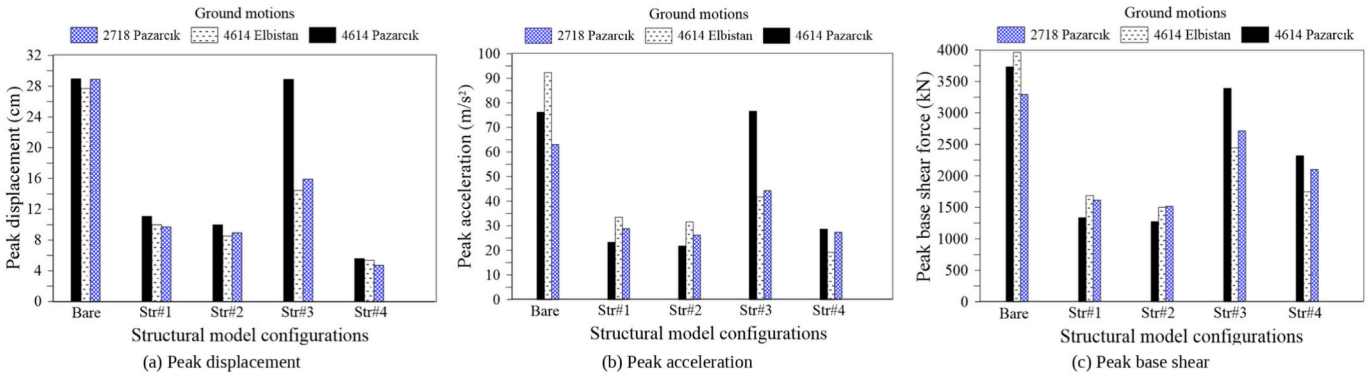

Fig. 20. Peak structural responses: (a) displacement (cm), (b) acceleration (cm/s^2), and (c) base shear (kN) for the bare and retrofitted configurations under the selected ground motions.

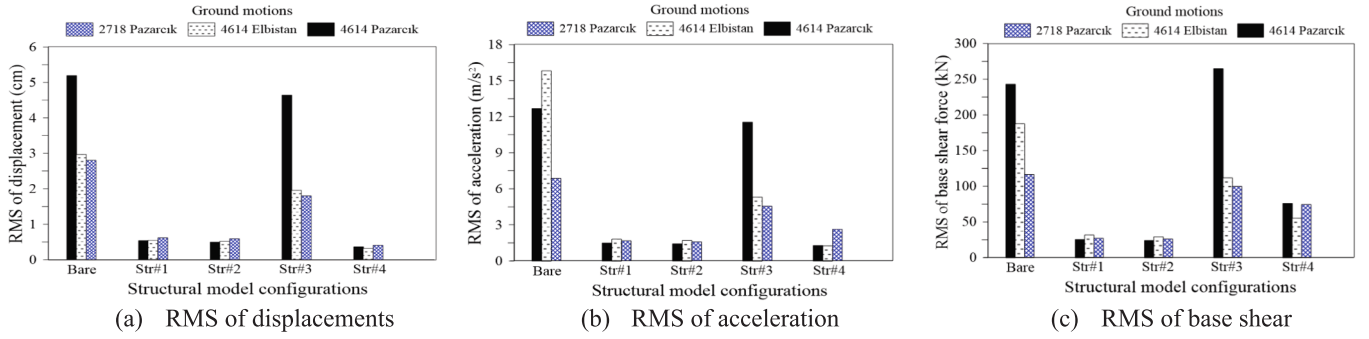

Fig. 21. RMS structural responses: (a) displacement (cm), (b) acceleration (cm/s^2), and (c) base shear (kN) under the selected ground motions.

and assigns the largest record-specific C_d to the external group. The assembled design is reanalysed under all records; final acceptance requires $D/C \leq 0.80$ for every audited member.

Phase B applies the response-based removal audit only to the retained external corner FVDs. For each corner device, $F_{d,i}^{env} = \max|F_{d,i,r}(t)|$ is calculated over the complete record set. The lowest-force device satisfying $F_{d,i}^{env} \leq F_{tol}$ is removed provisionally while the strengthened ring-beam sections and all other damper coefficients remain fixed. The reduced hybrid model is reanalysed under every record. If the complete audit fails, only the remaining external coefficients are increased using Eq. (5); the strengthening is not enlarged during the removal trial. If compensation cannot restore feasibility within the adopted bounds, the corner device is reinstated.

The Str#4-specific implementation is summarised in Fig. 18 and is given below; the common DM-II equations and safeguards in Section 3.2 govern each external-coefficient calibration or compensation stage.

Step 1. *Activate and initialize the external corner FVDs.* For the current record, activate only the external rock-to-column devices and assign $C_{d,initial}$. Do not install internal deck FVDs.

Step 2. *Run THA and evaluate the column-control group.* Perform THA, evaluate $\eta_{g,r}^{(m)}$ using Eq. (3), examine the column-region D/C values, and store the external-device demands.

Step 3. *Test external-group convergence.* Verify $0.784 \leq \eta_{g,r}^{(m)} \leq 0.800$. A NO result leads to Step 4; a YES result leads to Step 5.

Step 4. *Update the external coefficient and repeat THA.* Update the out-of-band external $C_{d,g,r}^{(m)}$ using Eq. (5), apply the numerical bounds, and return to Step 2.

Step 5. *Audit the deck without internal damping.* Keep the converged external coefficient and check every deck member. If every deck member satisfies $D/C \leq 0.80$, proceed to Step 11; otherwise proceed to Step 6.

Step 6. *Identify the governing deck demand.* For each member with $D/C > 0.80$, identify the governing region and determine whether the residual demand reflects local capacity, torsional distortion, or a distributed ring-beam mechanism.

Step 7. *Strengthen the governing ring-beam region.* Introduce the required section enhancement. For the Oylat platform, the final intervention consists of 40-mm side plates on both the inner and outer HE400B ring-beam systems.

Step 8. *Perform the coupled post-strengthening THA.* Reanalyze the deck and supporting system after each section change. Re-evaluate the deck and column-control regions and update the external force, stroke, and velocity demands.

Step 9. *Test the coupled hybrid targets.* Proceed to Step 11 only when the column-sizing condition is satisfied and every audited member has $D/C \leq 0.80$. Otherwise proceed to Step 10.

Step 10. *Refine damping and/or strengthening.* If the column index is out of band, update the external C_d using Eq. (5). If any deck member still has $D/C > 0.80$, increase the required strengthening extent. Repeat Step 8. The lower Eq. (4) limit is a damper-sizing tolerance and is not used to reduce an adequate strengthened section.

Step 11. *Form and verify the governing hybrid design.* Repeat Steps 1-10 for every record. Retain every required strengthening region, use the largest required extent at each region, and assign the largest record-specific external C_d. Reanalyse every record. Phase B begins only after the complete member and device-demand audits pass.

Step 12. *Calculate the external corner-damper force envelopes.* For every retained corner FVD, calculate $F_{d,i}^{env}$ over all analysis times and records. Internal devices are absent from Str#4 and the strengthened sections are not removal candidates.

Step 13. *Screen for a near-zero-force corner device.* Check whether any active corner FVD satisfies $F_{d,i}^{env} \leq F_{tol}$. If none does, proceed to Step 18. If both qualify, select only the device with the smaller envelope.

Table 3a
Member-level D/C distribution and record-level maximum for the 2718 Pazarcık ground motion.

Model	Member group	No. of members	Number of members within each D/C interval			Record-level maximum D/C
			D/C ≤ 0.60	0.60 < D/C ≤ 0.80	D/C > 0.80	
Bare	Outer circular ring beams	57	0	12	45	2.1824
	Inner circular ring beams	59	3	6	50	
	Radial beams	16	0	1	15	
	Primary deck beams	26	0	2	24	
	Diagonal bracing members	64	13	4	47	
	Vertical support columns	32	24	4	4	
	Inclined bracing members	8	8	0	0	
Str#1	Outer circular ring beams	57	57	0	0	0.7635
	Inner circular ring beams	59	43	16	0	
	Radial beams	16	16	0	0	
	Primary deck beams	26	26	0	0	
	Diagonal bracing members	64	55	9	0	
	Vertical support columns	32	32	0	0	
	Inclined bracing members	8	8	0	0	
Str#2	Outer circular ring beams	57	57	0	0	0.7403
	Inner circular ring beams	59	47	12	0	
	Radial beams	16	16	0	0	
	Primary deck beams	26	26	0	0	
	Diagonal bracing members	64	60	4	0	
	Vertical support columns	32	32	0	0	
	Inclined bracing members	8	8	0	0	
Str#3	Outer circular ring beams	57	24	23	10	1.5519
	Inner circular ring beams	59	15	4	40	
	Radial beams	16	11	5	0	
	Primary deck beams	26	24	2	0	
	Diagonal bracing members	64	54	10	0	
	Vertical support columns	32	32	0	0	
	Inclined bracing members	8	8	0	0	
Str#4	Outer circular ring beams	57	57	0	0	0.7882
	Inner circular ring beams	59	59	0	0	
	Radial beams	16	14	2	0	
	Primary deck beams	26	26	0	0	
	Diagonal bracing members	64	51	13	0	
	Vertical support columns	32	32	0	0	
	Inclined bracing members	8	5	3	0	

Table 3b
Member-level D/C distribution and record-level maximum for the 4614 Elbistan ground motion.

Model	Member group	No. of members	Number of members within each D/C interval			Record-level maximum D/C
			D/C ≤ 0.60	0.60 < D/C ≤ 0.80	D/C > 0.80	
Bare	Outer circular ring beams	57	0	2	55	4.2003
	Inner circular ring beams	59	3	0	56	
	Radial beams	16	0	0	16	
	Primary deck beams	26	0	0	26	
	Diagonal bracing members	64	12	4	48	
	Vertical support columns	32	19	5	8	
	Inclined bracing members	8	1	1	6	
Str#1	Outer circular ring beams	57	57	0	0	0.7383
	Inner circular ring beams	59	38	21	0	
	Radial beams	16	16	0	0	
	Primary deck beams	26	26	0	0	
	Diagonal bracing members	64	56	8	0	
	Vertical support columns	32	32	0	0	
	Inclined bracing members	8	8	0	0	
Str#2	Outer circular ring beams	57	57	0	0	0.6957
	Inner circular ring beams	59	45	14	0	
	Radial beams	16	16	0	0	
	Primary deck beams	26	26	0	0	
	Diagonal bracing members	64	59	5	0	
	Vertical support columns	32	32	0	0	
	Inclined bracing members	8	8	0	0	
Str#3	Outer circular ring beams	57	35	18	4	1.4283
	Inner circular ring beams	59	17	9	33	
	Radial beams	16	14	2	0	
	Primary deck beams	26	25	1	0	
	Diagonal bracing members	64	56	8	0	
	Vertical support columns	32	32	0	0	
	Inclined bracing members	8	8	0	0	
Str#4	Outer circular ring beams	57	57	0	0	0.6581
	Inner circular ring beams	59	59	0	0	
	Radial beams	16	16	0	0	
	Primary deck beams	26	26	0	0	
	Diagonal bracing members	64	57	7	0	
	Vertical support columns	32	32	0	0	
	Inclined bracing members	8	8	0	0	

Table 3c
Member-level D/C distribution and record-level maximum for the 4614 Pazarcık ground motion.

Model	Member group	No. of members	Number of members within each D/C interval			Record-level maximum D/C
			D/C ≤ 0.60	0.60 < D/C ≤ 0.80	D/C > 0.80	
Bare	Outer circular ring beams	57	0	1	56	2.5767
	Inner circular ring beams	59	3	0	56	
	Radial beams	16	0	1	15	
	Primary deck beams	26	0	0	26	
	Diagonal bracing members	64	12	11	41	
	Vertical support columns	32	24	4	4	
	Inclined bracing members	8	2	4	2	
Str#1	Outer circular ring beams	57	57	0	0	0.7991
	Inner circular ring beams	59	34	25	0	
	Radial beams	16	16	0	0	
	Primary deck beams	26	26	0	0	
	Diagonal bracing members	64	52	12	0	
	Vertical support columns	32	32	0	0	
	Inclined bracing members	8	8	0	0	
Str#2	Outer circular ring beams	57	57	0	0	0.7820
	Inner circular ring beams	59	39	20	0	
	Radial beams	16	16	0	0	
	Primary deck beams	26	26	0	0	
	Diagonal bracing members	64	53	11	0	
	Vertical support columns	32	32	0	0	
	Inclined bracing members	8	8	0	0	
Str#3	Outer circular ring beams	57	10	13	34	2.8292
	Inner circular ring beams	59	7	4	48	
	Radial beams	16	5	1	10	
	Primary deck beams	26	2	22	2	
	Diagonal bracing members	64	51	8	5	
	Vertical support columns	32	32	0	0	
	Inclined bracing members	8	8	0	0	
Str#4	Outer circular ring beams	57	57	0	0	0.7291
	Inner circular ring beams	59	59	0	0	
	Radial beams	16	16	0	0	
	Primary deck beams	26	16	10	0	
	Diagonal bracing members	64	55	9	0	
	Vertical support columns	32	32	0	0	
	Inclined bracing members	8	8	0	0	

Note: Member counts are grouped as D/C ≤ 0.60, 0.60 < D/C ≤ 0.80, and D/C > 0.80. The displayed distributions cover the seven principal member groups listed in the panels. Record-level maxima and target assessments are based on the complete exported member set, which additionally includes circumferential deck joists, the inner polygonal ring beam, secondary deck joists, and bottom-chord members. All maxima are reported to four decimal places.

Table 3d
Heat-map synthesis of record-specific maximum D/C ratios, across-record governing envelopes, and target assessment.

Model / Strategy	Maximum D/C by Ground Motion			Across-Record Maximum D/C	Governing Record	Target Assessment (D/C ≤ 0.80)
	2718 Pazarcık	4614 Elbistan	4614 Pazarcık			
Bare Model Unretrofitted reference	2.1824	4.2003	2.5767	4.2003	4614 Elbistan	✕ Not satisfied
Str#1 Global damping	0.7635	0.7383	0.7991	0.7991	4614 Pazarcik	✓ Satisfied
Str#2 Sequential damping	0.7403	0.6957	0.7820	0.7820	4614 Pazarcik	✓ Satisfied
Str#3 Column-priority damping	1.5519	1.4283	2.8292	2.8292	4614 Pazarcik	✕ Not satisfied
Str#4 Hybrid retrofit	0.7882	0.6581	0.7291	0.7882	2718 Pazarcik	✓ Satisfied

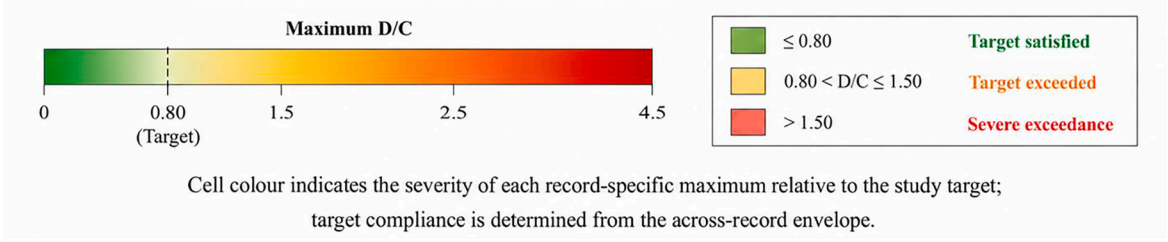

Note: The across-record maximum is the largest of the three record-specific maxima. Green cells denote D/C ≤ 0.80, amber cells denote 0.80 < D/C ≤ 1.50, and red cells denote D/C > 1.50. The target assessment is based on the across-record envelope; the associated critical members are identified in the accompanying discussion and conclusions.

Step 14. *Remove one corner device provisionally.* Deactivate only the selected lowest-force corner FVD. Keep the other C_d value and the complete strengthened-section layout unchanged.

Step 15. *Perform the mandatory post-removal THAs.* Reanalyze every selected record with the reduced external layout and fixed strengthened sections. Re-audit the complete member set and update the demand envelopes of the retained corner device.

Step 16. *Assess the trial removal.* Retain the removal only if every audited member satisfies $D/C \leq 0.80$ under every record and the retained device satisfies all practical limits. A successful trial leads to Step 18; otherwise proceeds to Step 17.

Step 17. *Compensate with the remaining external device.* Keep the candidate inactive and increase the remaining external C_d using Eq. (5). Repeat all-record THA and the complete audit, then return to Step 12 and recompute the corner-device envelope. If compensation is infeasible within the coefficient or device-demand bounds, reinstate the removed corner FVD and return to Step 12 with the last feasible hybrid design.

Step 18. *Accept the final Str#4 design.* Accept the latest verified hybrid configuration when Step 13 finds no eligible corner device or Step 16 confirms a successful trial. Save the retained external layout, strengthening details, final coefficients, and governing device demands; acceptance requires $D/C \leq 0.80$ for every audited member and every record.

4. Results and Discussion

4.1. Seismic displacement response of the bare model

Fig. 19 illustrates the horizontal displacement contours of the bare model under the three selected near-source motions. The peak horizontal displacements are 25.94 and 24.08 cm under 2718 Pazarcık, 26.11 and 23.55 cm under 4614 Elbistan, and 28.94 and 23.95 cm under 4614 Pazarcık. The 4614 Pazarcık motion therefore governs peak displacement only; the member-level D/C envelope is governed by 4614 Elbistan. Because no independent displacement acceptance limit is adopted in this study, the contours are used diagnostically rather than as a code-compliance test. They show large, asymmetric deformation extending from the supporting tower into the circular deck, particularly along the outer perimeter and access-side segment. This pattern is consistent with coupled tower–deck response and torsion-sensitive plan deformation and motivates simultaneous assessment of global support demand and local deck response.

4.2. Comparison of peak structural response parameters

Fig. 20 compares the peak responses of the bare and retrofitted configurations. Str#4 reduces base shear relative to the bare model. Its reduction is smaller than those of Str#1 and Str#2. A uniform period shortening does not explain this result. The global torsion-dominated first period increases from 1.197 to 1.416 s. The second and third periods decrease to 0.497 and 0.300 s. For the three matched records, the 5%-damped spectral accelerations at 1.197 s are about 0.578, 0.558, and 0.568 g. At 1.416 s, they are about 0.480, 0.372, and 0.507 g. Therefore, increased first-mode spectral acceleration or fundamental-mode pulse resonance does not cause the higher Str#4 base shear relative to Str#1 and Str#2. Several effects act together. These include greater deck mass and peripheral polar inertia, less local deck distortion, changed higher modes, and more direct force transfer through the strengthened deck–tower load path.

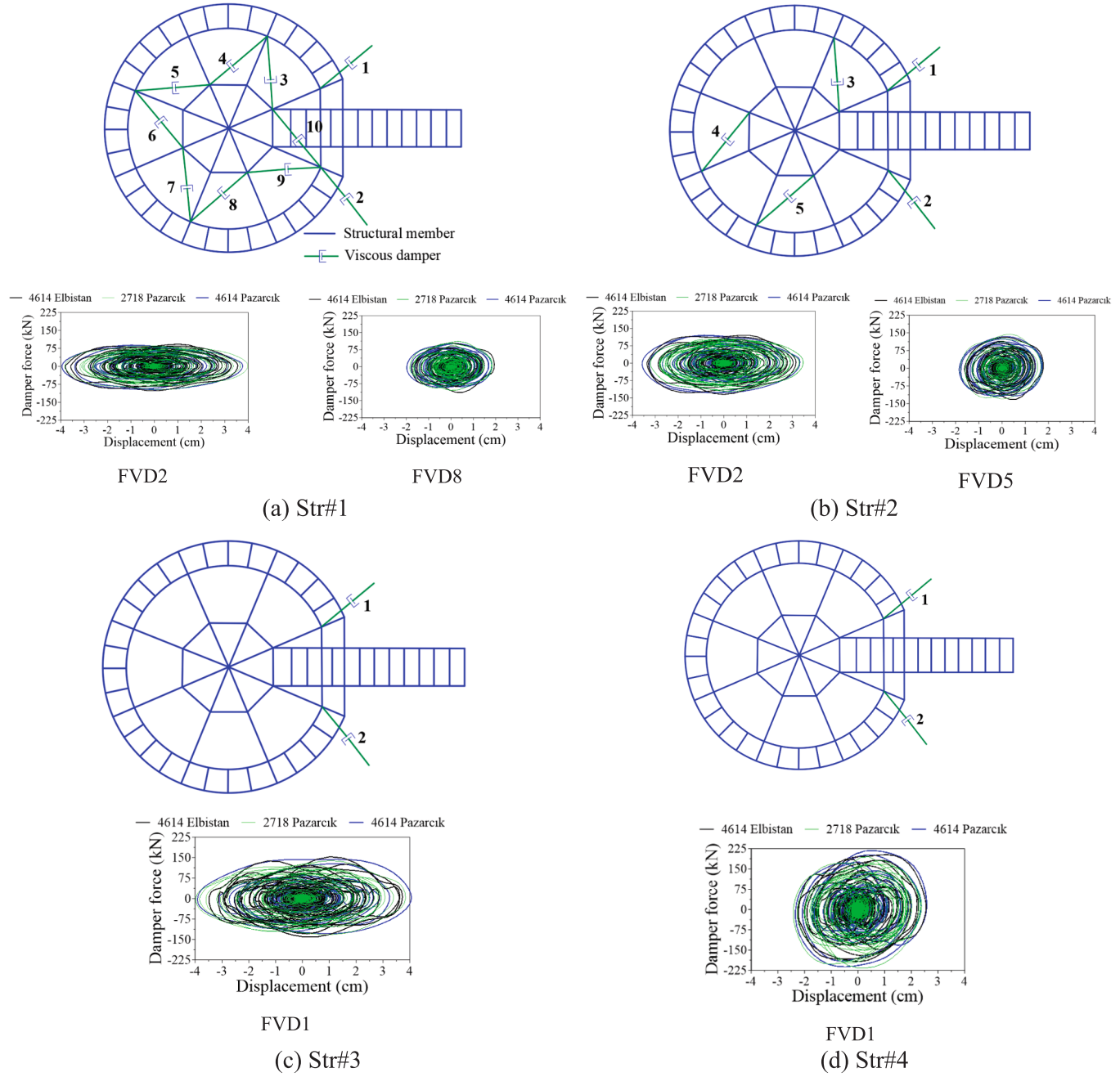

Fig. 22. Damper force–displacement hysteresis loops for (a) Str#1, (b) Str#2, (c) Str#3, and (d) Str#4; damper force is reported in kN and displacement in cm.

4.3. RMS-based response evaluation

Fig. 21 gives the root-mean-square (RMS) displacement, acceleration, and base shear. RMS is a time-averaged response measure over each record. It is not an energy measure, a cumulative-damage measure, or an acceptance rule. The bare model has the largest RMS displacement. Str#1, Str#2, and Str#4 reduce the time-averaged vibration. Str#3 retains relatively high RMS displacement because its deck demand remains untreated. The RMS acceleration and base-shear results have the same general order. Str#1 and Str#2 give the lowest sustained global response. Str#4 is intermediate, and Str#3 has the highest response among the retrofit cases. For these records, the RMS results support the peak-response and member-level results. They indicate that Str#2 is the most balanced damper-only case. They do not replace the D/C acceptance check.

4.4. Element-level performance assessment and strategy effectiveness

Tables 3a–c give the final member-level results for 2718 Pazarcık, 4614 Elbistan, and 4614 Pazarcık. The final across-record configuration is used in every case. Each panel uses the same model order, member-group order, D/C intervals, and four-decimal reporting. Table 3d compares the record-specific maxima with the across-record envelope and target. The bare-model maxima are 2.1824, 4.2003, and 2.5767. Str#1, Str#2, and Str#4 keep every audited member at D/C $\leq$ 0.80 under all records. Their across-record maxima are 0.7991, 0.7820, and 0.7882. Str#3 reaches 2.8292 under 4614 Pazarcık. This does not mean that its column-control iteration failed. Str#3 intentionally leaves the deck untreated and therefore does not meet the complete-system target.

The heat-map summary also clarifies the final safety margin after the across-record coefficient/intervention envelope has been imposed. Str#1 is closest to the adopted boundary, with a margin of only 0.0009

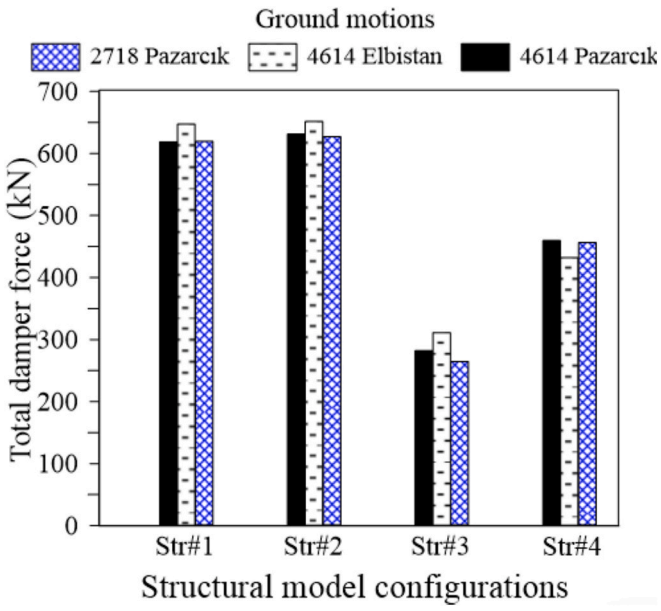

Fig. 23. Aggregate peak-force index for each selected record after the final configuration is applied. The index is the sum of individual peak absolute damper forces. These peaks may occur at different times. The index is not used to select Cd.

below D/C = 0.80; Str#4 retains a margin of 0.0118, while Str#2 provides the largest margin, 0.0180. The fact that several final record-specific maxima are below the 0.784 DM-II lower sizing bound is expected: Eq. (4) is applied during record-specific coefficient tuning, whereas the final configuration uses the maximum coefficient/intervention demand required across records and can therefore over-control non-governing motions. These small differences should not be interpreted as statistical rankings because only three matched motions are considered.

The strategies produced different results. Str#1 controlled the structure but used the largest predefined damper layout. Str#2 gave the lowest complete-member demand envelope. It first controlled the columns, then added deck dampers one at a time, and retuned the affected internal groups after each addition. Inner ring beam i7 governed Str#2 under 4614 Pazarcık. Str#3 achieved its column-control objective but left large deck demands because it included no deck intervention. Str#4 combined external dampers with ring-beam strengthening and removed all audited deck exceedances. These comparisons apply only to the present structure and record set.

4.5. Numerical damper force–displacement response

Fig. 22 shows the numerical damper force–displacement loops. Their enclosed areas indicate energy dissipation by the modelled velocity-dependent links. The devices are idealised linear Maxwell-type links. Therefore, the plots are analytical demand histories, not experimental proof of cyclic stability, durability, or qualification. Str#1 and Str#2 distribute damper demand among several critical locations. The wider FVD2 loops show larger relative displacement. The smaller FVD8 and FVD5 loops show more localised motion. Str#3 and Str#4 use the same external device location. Their loop shapes differ because the Str#4 section strengthening changes local deformation and force transfer. Device response therefore depends on both damper properties and the surrounding structural region.

4.6. Comparison of damper force demands across retrofit strategies

Fig. 23 compares the aggregate peak-force index for each record after the final configuration is applied. The index is the sum of the individual peak absolute damper forces from the final reanalysis. These peaks usually occur at different times. Therefore, the index is not an instantaneous resultant and must not be used as a connection force. Design must use the final force, stroke, and velocity envelope of each individual damper. The aggregate index is only a comparison measure. It does not select the final C_d values. Str#1 and Str#2 develop the largest aggregate peak-force indices because both external and internal devices participate in the response-control system. Str#2 is slightly more demanding for some records, but its sequential layout provides the most balanced reduction of displacement, acceleration, and base reaction among the damper-only alternatives. Str#3 exhibits the lowest index because it contains only the column-control device group; this lower value does not represent superior performance, since substantial deck-level D/C exceedances remain. The aggregate peak-force index cannot identify a removable damper because it discards device location and time-history information. Candidate screening instead uses the individual across-record envelope $F_{d,i}^{env}$ and the mandatory post-removal THA. This distinction is important for Str#2, whose external and internal devices participate in different control regions, and for Str#4, where only the corner FVDs are screened while the strengthened deck remains unchanged. Str#4 produces an intermediate aggregate peak-force index. The external dampers control the supporting system, while the strengthened ring beams reduce the need for additional internal deck dampers. This result illustrates how supplemental damping and targeted capacity enhancement can redistribute the device-demand burden. The index alone is neither a cost nor a safety metric: the number of devices, individual force, stroke, and velocity envelopes, connection and anchorage demands, installation access, and maintenance requirements must be evaluated separately.

4.7. Local displacement response of the outer circular deck region

Fig. 24 shows displacement along the outer circular deck line. This line is sensitive to plan distortion because it connects the radial beams, outer ring beam, eccentric access ramp, and tower support. This local measure complements the global peak and RMS results. Two configurations can have similar deck-centre displacement but different circumferential deformation and member demand. The bare model has the largest and most irregular circumferential displacement. This pattern is consistent with ovalisation and torsion-sensitive local amplification. Str#1 and Str#2 reduce the amplitude with supplemental damping. Str#1 activates and tunes the complete feasible deck-and-support layout at the same time. Str#2 controls the columns first. It then adds internal deck dampers one at a time and retunes the active deck groups after each addition. Both strategies satisfy the D/C target for every reported member. Their across-record maxima are 0.7991 and 0.7820. Str#3 retains large local deck peaks because it has no deck intervention. Str#4 gives the most uniform local deck response and has no target exceedance. Under 2718 Pazarcık, its platform maximum is 0.7800 in radial beam 4-rb1. Its complete-system maximum is 0.7882 in supporting diagonal brace 1-dbm7. Str#4 gives the most uniform outer-deck displacement profile. Two mechanisms produce this improvement. The external rock-to-column dampers reduce the velocity-dependent support response. The 40-mm side plates on the inner and outer HE400B ring beams increase local torsional stiffness and member capacity. The smaller local deformation is consistent with the lower deck demand. However, the added stiffness also changes the modal periods and force distribution. Both local demand and support reactions must therefore be checked after strengthening. The selected analyses show that global response reduction is not enough for a torsion-sensitive circular deck. Local displacement shape, member D/C, damper force, and support-force transfer must be considered together. Fig. 24 profiles support a case-specific conclusion. Distributed or sequential damping can control the global response. Targeted section strengthening may still

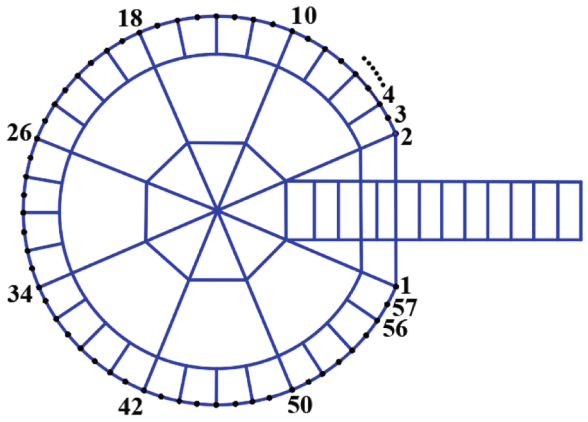

a) Outer circular radial beam joint number

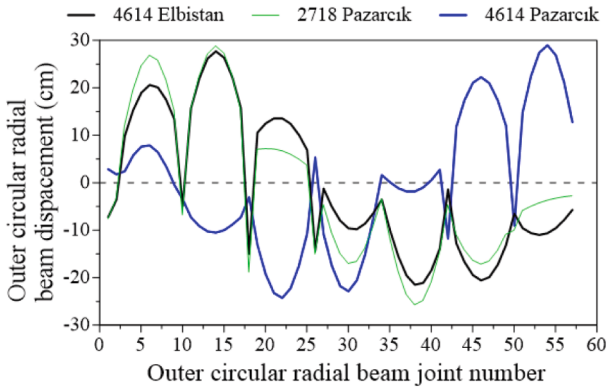

b) Bare Model

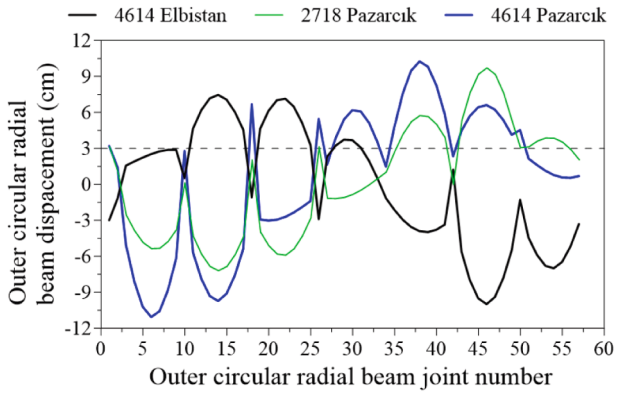

c) Str#1

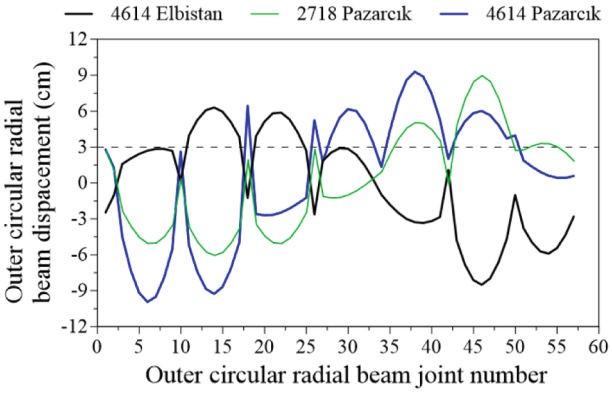

d) Str#2

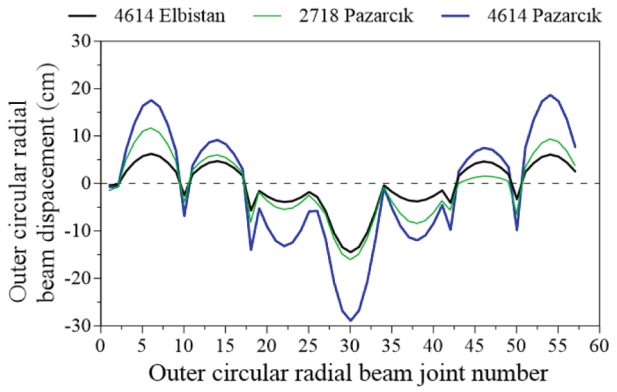

e) Str#3

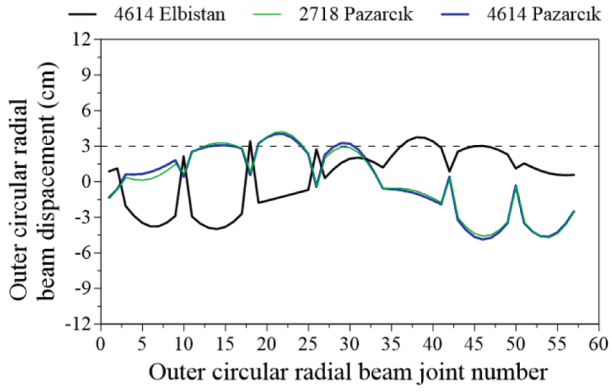

f) Str#4

Fig. 24. Outer circular deck displacement assessment: (a) monitored joint locations and displacement profiles for (b) the bare model, (c) Str#1, (d) Str#2, (e) Str#3, and (f) Str#4. Displacements are reported in cm.

be needed when local ring-beam deformation governs.

5. Conclusion

This study compared four record-specific retrofit strategies for the Oylat Glass Observation Platform under the same three spectrally matched near-source motions and the same study-specific D/C $\leq$ 0.80 target. The governing across-record coefficients and interventions were applied in the final reanalyses. The principal findings are as follows:

- The bare model showed large asymmetric and torsion-sensitive deformation. Its largest reported horizontal displacement was 28.94 cm under 4614 Pazarcık, whereas the member-demand envelope was governed by 4614 Elbistan at D/C = 4.2003. Because no independent displacement limit was adopted, displacement was used as a diagnostic response measure rather than a compliance criterion.
- Str#1, Str#2, and Str#4 satisfied D/C $\leq$ 0.80 for every audited member under all three records. Their across-record maxima were 0.7991, 0.7820, and 0.7882, respectively, corresponding to margins of 0.0009, 0.0180, and 0.0118 below the adopted target.
- Among the complete damper-based alternatives, Str#2 produced the lowest complete-member demand envelope. Its column-first, demand-guided deck allocation reduced both global response and local deck demand without activating the full predefined deck layout at

the outset. This ranking is case-specific and is not a direct measure of cost or statistical reliability.

- Str#3 achieved its intended vertical-column-control objective but did not provide a complete-system retrofit. The untreated deck retained extensive exceedances, and the across-record maximum reached D/C = 2.8292 under 4614 Pazarcık. This result demonstrates that satisfying one controlled subsystem does not establish whole-system acceptance after force redistribution.
- Str#4 combined external FVDs with 40-mm side-plate strengthening of the governing inner and outer HE400B ring-beam regions. It satisfied the complete-member target and produced the most uniform outer-deck displacement profile, while its altered periods and load path confirm that member demand and support reactions must be rechecked after stiffness modification.
- The aggregate peak-force index was useful only for strategy comparison; it is not an instantaneous connection force. Final device and connection design must use the individual force, stroke, and velocity envelopes and must recheck supporting members, welded attachments, anchorage, and foundation actions after every accepted redistribution.

These findings are limited to the linearly elastic member model, P–Delta geometric effects, idealised linear FVD links, equal-component biaxial excitation, and the three matched records used here. The reported coefficients, device demands, and strategy ordering should therefore be interpreted as a structure-specific proof of concept, not as generally calibrated design values.

6. Future Work

Future work should address the followings issues:

- Use larger suites of independent bidirectional ground-motion pairs from multiple events and examine component orientation, phase relation, record-to-record variability, and pulse sensitivity.
- Calibrate material-nonlinear models, including connection, support, foundation, and rock-anchor flexibility, and reassess the response measure, acceptance band, and coefficient-update rule for nonlinear response.
- Evaluate nonlinear FVDs with $0 < \alpha_d < 1$, including force saturation, stroke, velocity, temperature, durability, and failure modes.
- Compare the present deterministic iteration with different optimisation methods.

CRediT authorship contribution statement

Adnan Kiral: Methodology, Investigation, Formal analysis, Data curation. **Zeliha Tonyali:** Methodology, Investigation, Formal analysis, Data curation, Conceptualization. **Maziar Fahimi Farzam:** Supervision, Resources, Methodology.

Declaration of competing interest

The authors declare that they have no known competing financial interests or personal relationships that could have appeared to influence the work reported in this paper.

Acknowledgements

The authors gratefully acknowledge the financial support provided by the Recep Tayyip Erdogan University Development Foundation under Grant No. 02026008014567.

References

[1] A. Tadeu, A. Romero, F. Bandeira, F. Pedro, S. Dias, M. Serra, M. Brett, P. Galvín, Theoretical and experimental analysis of the quasi-static and dynamic behaviour of the world's longest suspension footbridge in 2020, Eng. Struct. 253 (2022) 113830, https://doi.org/10.1016/j.engstruct.2021.113830.
[2] M. Gong, R. Shen, Y. Li, H. Wang, W. Chen, X. Wei, Practical Suggestions for Specifications for the Vibration Serviceability of Footbridges Based on Two Recent Long-Span Footbridges, Struct. Eng. Int. 33 (4) (2023) 659–676, https://doi.org/10.1080/10168664.2022.2149376.
[3] Y. Li, X. Zhang, C. Wang, Y. Zhang, X. Wei, Human-induced vertical vibration of a glass suspension footbridge: experimental study and numerical analysis, Struct. Infrastruct. Eng. 21 (4) (2025) 656–674, https://doi.org/10.1080/15732479.2023.2230567.
[4] M. Çakır, Y. Tekin, A Spatial and Experiential Assessment of the Kirazlıdere Glass Observation Deck: Urban Integration and User Perception, GSI Journals Serie A: Advancements in Tourism Recreation and Sports Sciences 8 (2) (2025) 677–697, https://doi.org/10.53353/atrss.1723665.
[5] M. Setareh, Vibration studies of a cantilevered structure subjected to human activities using a remote monitoring system, J. Perform. Constr. Facil 25 (2) (2011) 87–97, https://doi.org/10.1061/(ASCE)CF.1943-5509.0000125.
[6] M. Setareh, Vibrations due to walking in a long-cantilevered office building structure, J. Perform. Constr. Facil 26 (3) (2012) 255–270, https://doi.org/10.1061/(ASCE)CF.1943-5509.0000188.
[7] Z. Zhang, T. Guo, K. Yang, F. Ma, A. Li, Simulation and measurement of human-induced vibrations of the Beijing Olympic watchtower with tuned mass dampers, J. Perform. Constr. Facil 31 (6) (2017) 04017095, https://doi.org/10.1061/(ASCE)CF.1943-5509.0001089.
[8] C. Bedon, Issues on the vibration analysis of in-service laminated glass structures: analytical, experimental and numerical investigations on delaminated beams, Appl. Sci. 9 (18) (2019) 3928, https://doi.org/10.3390/app9183928.
[9] M. Ergun, Z. Tonyali, A. Kiral, S. Elias, Resilience-oriented seismic retrofit of heritage masonry minarets using hybrid base isolation and supplemental damping, Structures 83 (2026) 110893, https://doi.org/10.1016/j.istruc.2025.110893.
[10] X. Chen, X. Geng, W. Fu, L. Tan, J. Guan, T. Liu, Vibration serviceability assessment of ribbon-shaped large-span footbridge at high altitudes under wind-pedestrians coupling effects, Structures 66 (2024) 106885, https://doi.org/10.1016/j.istruc.2024.106885.
[11] X. Dai, X. Wei, L. Tang, Z. Xue, Y. Wu, Vibration suppression of footbridges using nonlinear vertical absorbers, Int. J. Mech. Sci. 313 (2026) 111309, https://doi.org/10.1016/j.ijmecsci.2026.111309.
[12] L. Gaile and I. Radinsh, "Steel lattice sightseeing tower's horizontal vibrations induced by human movement," in *Proceedings of the 25th International Conference on Noise and Vibration Engineering (ISMA2012/USD2012)*, Leuven, Belgium, September 17–19, 2012, pp. 1211–1221.
[13] Y. Li, P. Feng, J.-X. Xiao, M. Chen, J.-W. Li, Experimental investigations on the influence of bridge deck gratings on the aerodynamic stability of the long-span suspension footbridge with a streamlined double-side box girder, J. Wind Eng. Ind. Aerodyn. 254 (2024) 105904, https://doi.org/10.1016/j.jweia.2024.105904.
[14] C. Lu, J. Xia, X. Wang, K. Wen, Q. Wang, Q. Liu, Analysis of human-induced vibration response and TLD vibration reduction of high fundamental frequency aluminum alloy footbridge, Structures 70 (2024) 107579, https://doi.org/10.1016/j.istruc.2024.107579.
[15] M. Zhang, H. Yu, Z. Zhang, and F. Xu, "Vortex-induced vibration control of bridge decks using energy dissipative devices: A review of recent developments," *Advances in Wind Engineering*, vol. 2, no. 3, Art. no. 100069, 2025. doi: 10.1016/j.awe.2025.100069.
[16] M.F. Farzam, H.H. Jalali, Tandem tuned mass damper inerter for passive control of buildings under seismic loads, Struct. Control Health Monit. 29 (9) (2022) e2987.
[17] S. Elias, V. Matsagar, Research developments in vibration control of structures using passive tuned mass dampers, Annu. Rev. Control. 44 (2017) 129–156, https://doi.org/10.1016/j.arcontrol.2017.09.015.
[18] Z. Shu, R. You, Y. Zhou, Viscoelastic Materials for Structural Dampers: A Review, Constr. Build. Mater. 342 (2022) 127955, https://doi.org/10.1016/j.conbuildmat.2022.127955.
[19] A.S. Saeed, R. Abdul Nasar, M.A. Al-Shudeifat, A review on nonlinear energy sinks: designs, analysis and applications of impact and rotary types, Nonlinear Dyn. 111 (1) (2023) 1–37, https://doi.org/10.1007/s11071-022-08094-y.
[20] D. De Domenico, G. Ricciardi, I. Takewaki, Design strategies of viscous dampers for seismic protection of building structures: a review, Soil Dyn. Earthq. Eng. 118 (2019) 144–165, https://doi.org/10.1016/j.soildyn.2018.12.024.
[21] C.M. Villanueva, O.D. Cruz, The application of nonlinear fluids viscous dampers in resilience-based seismic design: A systematic review, Structures 74 (2025) 108538, https://doi.org/10.1016/j.istruc.2025.108538.
[22] A.E. Çerçevik, Ö. Avşar, A. Dilsiz, Optimal placement of viscous wall dampers in RC moment resisting frames using metaheuristic search methods, Eng. Struct. 249 (2021) 113108, https://doi.org/10.1016/j.engstruct.2021.113108.
[23] Y. Zhou, P. Chen, D. Zhang, S. Gong, W. Lu, A new analytical model for viscous wall dampers and its experimental validation, Eng. Struct. 163 (2018) 224–240, https://doi.org/10.1016/j.engstruct.2018.02.049.
[24] H. Gao, H. Wang, J. Li, Z. Wang, R. Liang, Z. Xu, Y. Ni, Optimum design of viscous inerter damper targeting multi-mode vibration mitigation of stay cables, Eng. Struct. 226 (2021) 111375, https://doi.org/10.1016/j.engstruct.2020.111375.
[25] K. Ikago, K. Saito, N. Inoue, Seismic control of single-degree-of-freedom structure using tuned viscous mass damper, Earthquake Engineering & Structural Dynamics 41 (3) (2012) 453–474, https://doi.org/10.1002/eqe.1138.

[26] Z. Xu, A. Agrawal, W.-L. He, P. Tan, Performance of passive energy dissipation systems during near-field ground motion type pulses, Eng. Struct. 29 (2) (2007) 224–236, https://doi.org/10.1016/j.engstruct.2006.04.020.
[27] A. Ras, N. Boumechra, Seismic energy dissipation study of linear fluid viscous dampers in steel structure design, Alex. Eng. J. 55 (3) (2016) 2821–2832, https://doi.org/10.1016/j.aej.2016.07.012.
[28] R.J. McNamara, D.P. Taylor, Fluid viscous dampers for high-rise buildings, Struct. Design Tall Spec. Build. 12 (2) (2003) 145–154, https://doi.org/10.1002/tal.218.
[29] D.P. Taylor, Smart buildings and viscous dampers—a design engineer's perspective, Struct. Design Tall Spec. Build. 19 (4) (2010) 369–372, https://doi.org/10.1002/tal.621.
[30] V. Nguyen-Thai, D.-K. Ly, T. Nguyen, and T. Nguyen-Thoi, "An effective optimum design for passive viscous damping control using FVDs/VWDs in multi-story buildings," *Structures*, vol. 67, Art. no. 107004, 2024. doi: 10.1016/j.istruc.2024.107004.
[31] A. Kiral, A. Gurbuz, I. Ustabas, The Seismic Response Evaluation of an Existing Multi-span Reinforced Concrete Highway Bridge in the Presence of Linear and Nonlinear Viscous Dampers, Arab. J. Sci. Eng. 50 (11) (2025) 8317–8335, https://doi.org/10.1007/s13369-024-09265-2.
[32] A. Kiral, Z. Tonyali, The effect of LRB stiffness changes with and without supplemental viscous dampers on seismic responses of an experimentally verified mdof building, Sigma Journal of Engineering and Natural Sciences 43 (1) (2025) 301–315, https://doi.org/10.14744/sigma.2024.00104.
[33] M. Gong, Y. Li, R. Shen, X. Wei, Glass suspension footbridge: human-induced vibration, serviceability evaluation, and vibration mitigation, J. Bridg. Eng. 26 (11) (2021) 05021014, https://doi.org/10.1061/(ASCE)BE.1943-5592.0001788.
[34] A. Ihsan Turan, A. Celik, A. Kumbasaroglu, and H. Yalciner, "Assessment of reinforced concrete building damages following the Kahramanmaraş earthquakes in Malatya, Turkey (February 6, 2023)," *Engineering Science and Technology, an International Journal*, vol. 54, p. 101718, 2024. doi: 10.1016/j.jestch.2024.101718.
[35] M.L. Ivanov, W.-K. Chow, Structural damage observed in reinforced concrete buildings in Adiyaman during the 2023 Turkiye Kahramanmaras Earthquakes, Structures 58 (2023) 105578, https://doi.org/10.1016/j.istruc.2023.105578.
[36] İ. Kazaz, İ.H. Bilge, M. Gürbüz, Near-fault ground motion characteristics and its effects on a collapsed reinforced concrete structure in Hatay during the February 6, 2023 Mw7.8 Kahramanmaraş earthquake, Eng. Struct. 298 (2024) 117067, https://doi.org/10.1016/j.engstruct.2023.117067.
[37] E. Güler, Non-linear site response and liquefaction analysis of soil site in Kahramanmaras during the *Mw* 7.7 and *Mw* 7.6 Turkey earthquakes, Engineering Science and Technology, an International Journal 57 (2024) 101751, https://doi.org/10.1016/j.jestch.2024.101751.
[38] Z. Qu, B. Zhu, Y. Cao, H. Fu, Rapid report of seismic damage to buildings in the 2022 M 6.8 Luding earthquake, China, Earthquake Res. Adv. 3 (1) (2023) 100180, https://doi.org/10.1016/j.eqrea.2022.100180.
[39] H. Gao, H. Chen, Y. Pan, X. Lai, Effects of horizontal pulse-like ground motions on a full-scale two-story RC frame with viscous fluid dampers: Shaking table tests, Soil Dyn. Earthq. Eng. 201 (2026) 109959, https://doi.org/10.1016/j.soildyn.2025.109959.
[40] Z. Tonyali, A. Kiral, M. Ergun, and R. Garcia, "Seismic resilience of existing RC dual-system buildings during the 2023 Kahramanmaraş earthquakes: a case study," *Journal of Asian Architecture and Building Engineering*, pp. 1–26, 2026. doi: 10.1080/13467581.2025.2564110.
[41] S. Avğın, M.M. Köse, A. Özbek, Damage assessment of structural and geotechnical damages in Kahramanmaraş during the February 6, 2023 earthquakes, Engineering Science and Technology, an International Journal 57 (2024) 101811, https://doi.org/10.1016/j.jestch.2024.101811.
[42] A. Kiral, Z. Tonyali, M. Ergun, A comprehensive analysis of the ground motions of the 2023 Kahramanmaraş, Türkiye earthquakes, Earthquakes Struct. 28 (3) (2025) 203–219, https://doi.org/10.12989/eas.2025.28.3.203.
[43] D. S. Panella, M. E. Tornello, C. D. Frau, A simple and intuitive procedure to identify pulse-like ground motions, Soil Dyn. Earthq. Eng. 94 (2017) 234–243, https://doi.org/10.1016/j.soildyn.2017.01.020.
[44] B. Dong, J.M. Ricles, B.M. Phillips, Experimental investigation of pulse-type ground motion effects on a steel building with nonlinear viscous dampers, Earthquake Engineering & Structural Dynamics 50 (15) (2021) 4032–4050, https://doi.org/10.1002/eqe.3544.
[45] P. Tan, A. Agrawal, Y. Pan, Near-field effects on seismically excited highway bridge equipped with nonlinear viscous dampers, Bridge Struct. 1 (3) (2005) 307–318, https://doi.org/10.1080/15732480500272718.
[46] Y. Yazdani, M. Alembagheri, Nonlinear seismic response of a gravity dam under near-source ground motions and equivalent pulses, Soil Dyn. Earthq. Eng. 92 (2017) 621–632, https://doi.org/10.1016/j.soildyn.2016.11.003.
[47] M. Akköse, E. Şimşek, Non-linear seismic response of concrete gravity dams to near-source ground motions including dam-water-sediment-foundation interaction, App. Math. Model. 34 (11) (2010) 3685–3700, https://doi.org/10.1016/j.apm.2010.03.019.
[48] W.-I. Liao, C.-H. Loh, B.-H. Lee, Comparison of dynamic response of isolated and non-isolated continuous girder bridges subjected to near-source ground motions, Eng. Struct. 26 (14) (2004) 2173–2183, https://doi.org/10.1016/j.engstruct.2004.07.016.
[49] Disaster and Emergency Management Presidency of Türkiye (AFAD), "Türkiye Earthquake Hazard Map," interactive web application. [Online]. Available: https://tdth.afad.gov.tr/ (accessed 1 August 2026).
[50] Computers and Structures, Inc., *SAP2000: Integrated Software for Structural Analysis and Design*, Version 20.2.0, Berkeley, CA, USA.
[51] American Institute of Steel Construction (AISC), *Specification for Structural Steel Buildings (ANSI/AISC 360-10)*, Chicago, IL, USA, 2010.
[52] Taylor Devices, Inc., "Shock and vibration control products and engineering resources." [Online]. Available: https://www.taylordevices.com/ (accessed 1 August 2026).
[53] B. Dong, R. Sause, J.M. Ricles, Modeling of nonlinear viscous damper response for analysis and design of earthquake-resistant building structures, Bull. Earthq. Eng. 20 (2022) 1841–1864, https://doi.org/10.1007/s10518-021-01306-7.
[54] F. Scozzese, L. Gioiella, A. Dall'Asta, L. Ragni, and E. Tubaldi, "Influence of viscous dampers' ultimate capacity on the seismic reliability of building structures," *Structural Safety*, vol. 91, Art. no. 102096, 2021. doi: 10.1016/j.strusafe.2021.102096.
[55] B. Dong, R. Sause, and J. M. Ricles, "Seismic response and damage of reduced-strength steel MRF structures with nonlinear viscous dampers," *Journal of Structural Engineering*, vol. 144, no. 12, Art. no. 04018221, 2018. doi: 10.1061/(ASCE)ST.1943-541X.0002226.
[56] European Committee for Standardization (CEN), *EN 1993-1-8:2024, Eurocode 3—Design of Steel Structures—Part 1-8: Joints*, Brussels, Belgium, 2024.
[57] European Committee for Standardization (CEN), *EN 1090-2:2018+A1:2024, Execution of Steel Structures and Aluminium Structures—Part 2: Technical Requirements for Steel Structures*, Brussels, Belgium, 2024.
[58] European Committee for Standardization (CEN), EN 1993-1-1:2022, Eurocode 3—Design of Steel Structures—Part 1-1: General Rules and Rules for Buildings, Brussels, Belgium, 2022.
[59] J.L. Gross, Experimental study of gusseted connections, Engineering Journal, AISC 27 (1990) 89–97.
[60] B. Dowswell, Design for gusset plate buckling with variable stress trajectories, Engineering Journal 56 (3) (2019) 133–148, https://doi.org/10.62913/engj.v56i3.1153.
[61] Seismosoft Ltd., *SeismoMatch: A Computer Program for Spectrum Matching of Earthquake Records*, Version 2025, Pavia, Italy, 2025.
[62] J. Hancock, J. Watson-Lamprey, N.A. Abrahamson, J.J. Bommer, A. Markatis, E. McCoy, R. Mendis, An improved method of matching response spectra of recorded earthquake ground motion using wavelets, J. Earthq. Eng. 10 (spec01) (2006) 67–89, https://doi.org/10.1080/13632460609350629.
[63] L. Al Atik, N. Abrahamson, An improved method for nonstationary spectral matching, Earthq. Spectra 26 (3) (2010) 601–617, https://doi.org/10.1193/1.3459159.